Canadian Journal of Earth Sciences

OPEN ACCESS | Research Article

Silurian mafic magmatism related to post-collisional extension, Appalachian orogen, western Newfoundland

A.M. Hinchey[a], **J.G. Hinchey**[a], **H.A. Sandeman**[a], **C.J. Lissenberg**[b], **N. Rayner**[c], **and D. Mendoza Marin**[a]

[a]Geological Survey, Department of Energy and Mines, Government of Newfoundland and Labrador, P.O. Box 8700, St. John's, NL A1B 4J6, Canada; [b]School of Earth and Environmental Sciences, Cardiff University, Cardiff, UK; [c]Natural Resources Canada, Geological Survey of Canada, 601 Booth Street, Ottawa, ON K1A 0E8, Canada

Corresponding author: **A.M. Hinchey** (email: alanahinchey@gov.nl.ca)

Abstract

Gabbroic intrusions provide direct evidence of magmatic processes operating within the lithosphere and at the lithosphere–asthenosphere boundary, offering insights into magmatic differentiation, crustal growth, mantle–crust interaction, and tectonic evolution. The Taylor Brook Gabbro Suite (TBGS) is the northwesternmost expression of middle Silurian magmatism in the northern Appalachians. The petrogenesis and geochemical characteristics of the TBGS and crosscutting silicic magmatism are explored through U–Pb geochronology, mineral chemistry, lithogeochemistry, and Sr–Nd isotopic analyses, illustrating a complex history of mantle-derived mafic magmatism. The U–Pb zircon sensitive high-resolution ion microprobe ages indicate that, although the intrusive history is complex, the TBGS represents a magmatic event at 431.0 ± 2.7/4.3 Ma that was subsequently intruded by silicic magmatism at 419.7 ± 3.0/4.5 Ma. The mineral chemistry and lithogeochemistry of the TBGS suggest fractional crystallization of a magmatic system as the primary differentiation mechanism. The TBGS is tholeiitic and transitional to calc-alkaline and consists of non-arc-like, continental magmas derived from an enriched mid-ocean ridge basalt-like source. The silicic samples are granitic, magnesian, and alkali calcic in composition. The isotopic signatures of the TBGS are mostly juvenile with $\varepsilon Nd_{(430\ Ma)}$ ranging from −1.1 to +6.4 and $^{87}Sr/^{86}Sr_{(i)}$ values ranging from 0.703373 to 0.708250, with one sample having an $\varepsilon Nd_{(430\ Ma)}$ of −8.6, indicating a minor role of crustal contamination by Mesoproterozoic to Neoproterozoic basement rocks. Magma ascent may have utilized inherited deep crustal structures, such as the precursor to the Doucers Valley Fault/Long Range-Cabot Fault systems. Lithospheric extension likely caused by slab rollback created a window that allowed for asthenospheric upwelling, inducing partial melting and generation of the TBGS magmas.

Key words: Silurian mafic magmatism, Newfoundland, Appalachian orogen, Salinic orogeny, gabbro

1. Introduction

The northern Appalachian orogen preserves the closing of the Iapetus and Rheic Oceans and their associated marginal seaways, leading to the collision of composite Laurentia and western Gondwana during the Alleghenian (Murphy et al. 2010; van Staal and Barr 2012; Waldron et al. 2022). Newfoundland preserves evidence of these ocean closures, as recorded by several orogenic cycles: Taconic, Salinic, and Acadian (see Williams 1995; Hatcher 2010). The late Silurian to middle Devonian (Salinic and Acadian) orogenic events resulted in extensive magmatism across Newfoundland, which is interpreted to have migrated across the orogen as a result of progressive shallowing of slab subduction (Murphy et al. 1999; van Staal and Barr 2012; van Staal et al. 2014; Wang et al. 2024).

Newfoundland is dissected by major strike-slip to transtensional faults that are long-lived, complex, crustal-scale features that were initiated and reactivated throughout Appalachian orogenesis (Fig. 1). These faults controlled lateral, orogen-parallel transport of microcontinents and terranes (Waldron et al. 2015; van Staal et al. 2021). In western Newfoundland, the Long Range-Cabot Fault (LR-CF) system is thought to record major net dextral strike-slip movement (~200–300 km) of the Dashwoods terrane\Notre Dame arc along the Laurentian margin during Ordovician to Carboniferous (Brem 2007; Lin et al. 2013; van Staal and Zagorevski 2022). Seismic reflection data support the interpretation that the LR-CF system is a crustal-scale discontinuity (i.e., deep transcurrent fault), which may have originated during oblique convergence and terrane accretion during Taconic to Acadian orogenesis (Stockmal et al. 1990; Waldron and Stockmal 1994; Barr et al. 2014). Inherited deep crustal structures have been shown to repeatedly serve as zones of deformation and reactivation during orogenesis (Thomas 2006; Hatcher 2010; Guillaume et al. 2022).

The Laurentian margin is preserved in western Newfoundland as part of the Humber Zone and is separated by the LR-CF system from metamorphic equivalents of the marginal strata, interpreted to have been deposited on the hyperextended Laurentian margin and various microcontinents that

Fig. 1. Simplified geological map of Newfoundland showing the location of the Taylor Brook Gabbro Suite relative to major geological terranes and tectonic boundaries. The location of the Long Range Inlier relative to the Grenville Province in eastern Labrador is illustrated in the inset map. Beothuk Lake Line (BLL, formally Red Indian Line) nomenclature is from van Staal et al. (2024). Abbreviations: BDF, Baie d'Est Fault; DVF, Doucers Valley Fault system; DRG, Devils Room granite; GBF, Green Bay Fault; GHF, Gunflap Hills Fault; GL, Gander Lake subzone; LRI, Long Range Inlier; MC, Mount Cormack subzone; MMLg, Mic Mac Lake Group; MP, Meelpaeg; NAF, Northern Arm Fault; NPL, Noel Paul's Line; TBGS, Taylor Brook Gabbro Suite; Vlsz, Valentine Lake shear zone; Sz, subzone. Modified after Colman-Sadd et al. (1990), Hinchey (2010), and Sandeman et al. (2024).

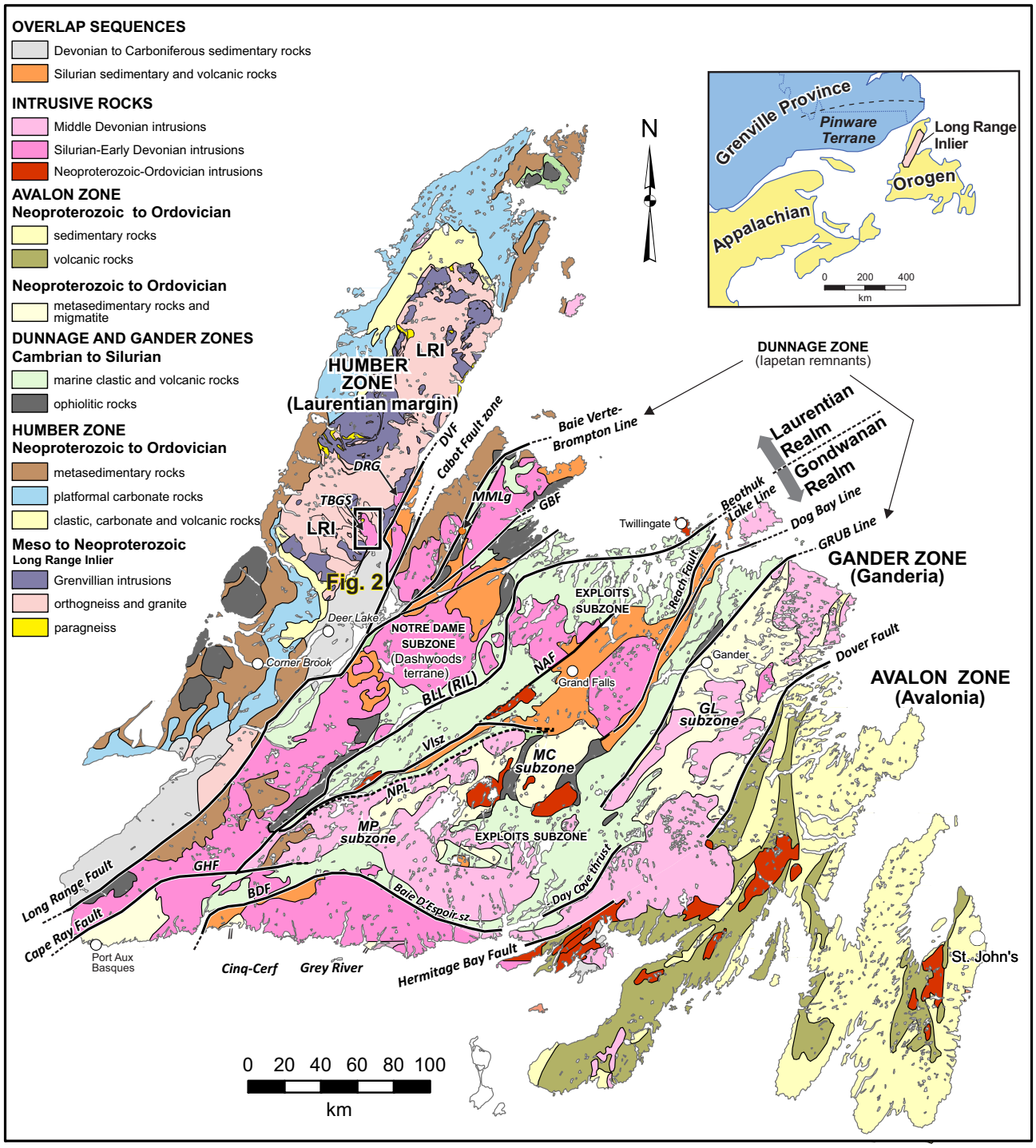

are now preserved within the Notre Dame arc/Dashwoods terrane (Laurentian Realm; Fig. 1). The Doucers Valley Fault (DVF) system is a subsidiary of the LR-CF system and apparently controlled the emplacement of Ordovician ophiolitic slices (Southern White Bay Allochthon), deposition of Silurian cover sequences, and focused Silurian magmatism in the White Bay region at the Humber margin–Dashwoods terrane boundary (Dunning 1987; Sandeman et al. 2024).

This paper presents U–Pb geochronology, mineral chemistry, lithogeochemistry, and Sr–Nd isotopic data from Silurian magmatic rocks that intrude the Humber margin of Newfoundland along the DVF system. The mafic intrusive rocks are of particular interest because they provide petrological constraints on mantle sources and contemporaneous geotectonic evolution. Thus, these rocks can provide key insights into the mantle sources beneath the northeastern Appalachian segment of the continental crust. The objectives here are (a) document the geology, petrology, and ages of the magmatic rocks; (b) elucidate the processes influencing their major and trace element compositions; (c) describe the geochemical characteristics of the magma sources and; (d) evaluate the degree to which lithospheric/crustal contamination influenced the parental magmas.

2. Geological setting

2.1. Regional tectonic framework

Historically, Newfoundland is divided from west to east into four tectonostratigraphic zones, namely, the Humber, Dunnage (Notre Dame/Dashwoods and Exploits terranes), Gander, and Avalon zones based on lithologic, paleontological, and lithogeochemical contrasts in pre-Silurian rocks (Fig. 1). The Gander and Avalon zones preserve remnants of different peri-Gondwana-derived terranes (Waldron et al. 2022). The Dunnage Zone contains the remnants of various continental and oceanic arc terranes that formed ribbons in the Iapetus Ocean, either as peri-Laurentian tectonic elements (Dashwoods terrane/Notre Dame arc) or peri-Ganderian tectonic elements (van Staal and Zagorevski 2022). The Humber Zone (or margin, see van Staal and Barr 2012) preserves deformed early Paleozoic passive-margin successions that were deposited on Laurentia (on the western margin of the Iapetus Ocean), above Mesoproterozoic to early Neoproterozoic (Tonian) basement of the Grenville Province (Long Range Inlier; Fig. 2). The Taylor Brook Gabbro Suite (TBGS), the focus of this study, intrudes the Long Range Inlier and is described in detail in the subsequent section.

2.2. Geology of the Long Range Inlier

The Long Range Inlier of western Newfoundland comprises one of the largest exposures of Proterozoic crystalline rocks within the Appalachian orogen. It is not a simple stratigraphic inlier but represents a massif reactivated during Appalachian orogenesis. The approximately 8500 km^2 massif comprises the largest portion of the external Humber Zone (Owen 1991). The Long Range Inlier forms a structural culmination bounded to the north, south, and locally to the east by Proterozoic to Paleozoic cover rocks. The western boundary is marked by a southeast-dipping thrust fault (the Long Range frontal thrust) that placed (i.e., back thrust) Proterozoic crystalline rocks onto autochthonous Cambro-Ordovician platformal strata and Taconic allochthonous rocks (Owen 1991; Erdmer and Williams 1995). Paleozoic deformation of the inlier is marked by low-grade metamorphism and tectonic overprinting along the DVF system and followed by emplacement of several intrusions, e.g., Devils Room granite, Gull Lake Intrusive Suite, and the TBGS. The DVF system, a part of the LR-CF system, marks wide tectonic zones of anastomosing ductile and brittle–ductile shear zones that are crosscut and overprinted by intense high-level brittle–ductile and brittle structures, largely obliterating the earlier ductile deformation structures. These faults and shear zones are long-lived, complex, crustal-scale features that were likely reactivated throughout the late Paleozoic assembly of the supercontinent Pangea (Smyth and Schillereff 1982; Hyde et al. 2007; Hinchey et al. 2022; Sandeman et al. 2024). Beginning in the Late Devonian, net dextral displacement along the LR-CF system is estimated at 200–300 km (Waldron et al. 2015).

The Long Range Inlier is largely composed of amphibolite to granulite facies orthogneiss with minor paragneiss. Greenschist facies rocks increase in areal extent eastwards towards the DVF system. The geology is broadly divisible into the following tectonic divisions: (1) high-grade ca. 1530–1466 Ma Long Range Gneiss Complex; (2) weakly to strongly foliated late Grenvillian plutonic rocks defining two temporal periods (ca. 1032–1022 and 993–985 Ma); (3) mafic dykes (the ca. 615 Ma Long Range dyke swarm); (4) thin structural remnants of latest Neoproterozoic to Paleozoic cover sequences; and (5) Early Silurian gabbroic intrusions and minor silicic intrusions with volcanic equivalents (Figs. 1 and 2; Owen 1991; Kamo et al. 1994; Heaman et al. 2002; Hinchey 2020; Hinchey et al. 2025).

2.3. Silurian magmatism

West of the DVF system, the only known expression of Silurian magmatism is the TBGS, with one thermal ionization mass spectrometry (TIMS) multigrain, U–Pb zircon age of 430.5 ± 2.5 Ma (Heaman et al. 2002), and the Devils Room granite (a poorly constrained, discordant, single bulk zircon age of 425 ± 10 Ma; Heaman et al. op. cit.). Aside from both intruding the Long Range Inlier, there is little previous research on either intrusion. East of the DVF system, there are Telychian (ca. 434 Ma) to Homerian (ca. 429 Ma) volcanosedimentary rocks of the Sops Arm Group (Sandeman and Dunning 2016; Sandeman et al. 2024) as well as the Gull Lake Intrusive Suite that has a poorly constrained U–Pb TIMS age of 398 + 27/−7 Ma (Erdmer 1986).

3. Methodology

This study integrates bedrock mapping, geochronology, petrography, thin section imagery, whole-rock lithogeochemistry, mineral chemistry, and whole-rock Sr–Nd isotopic data. Representative samples were examined petrographically using polished thin sections. Details of the methodology are in supplemental material A. Imaged thin sections (photomicrographs, canning electron microscopy–mineral liberation analysis maps, and XRF elemental maps) are presented in supplemental material B and Fig. 4. The U–Pb sensitive high-resolution ion microprobe (SHRIMP) zircon data are reported in supplemental material C. Cathodoluminescence (CL) images of analyzed zircon grains are presented in supplemental material D. Mineral chemical analyses are presented in sup-

Fig. 2. Geology of the Silver Mountain map area. Modified after Hinchey (2020). U/Pb zircon ages from Heaman et al. (2002) and this study.

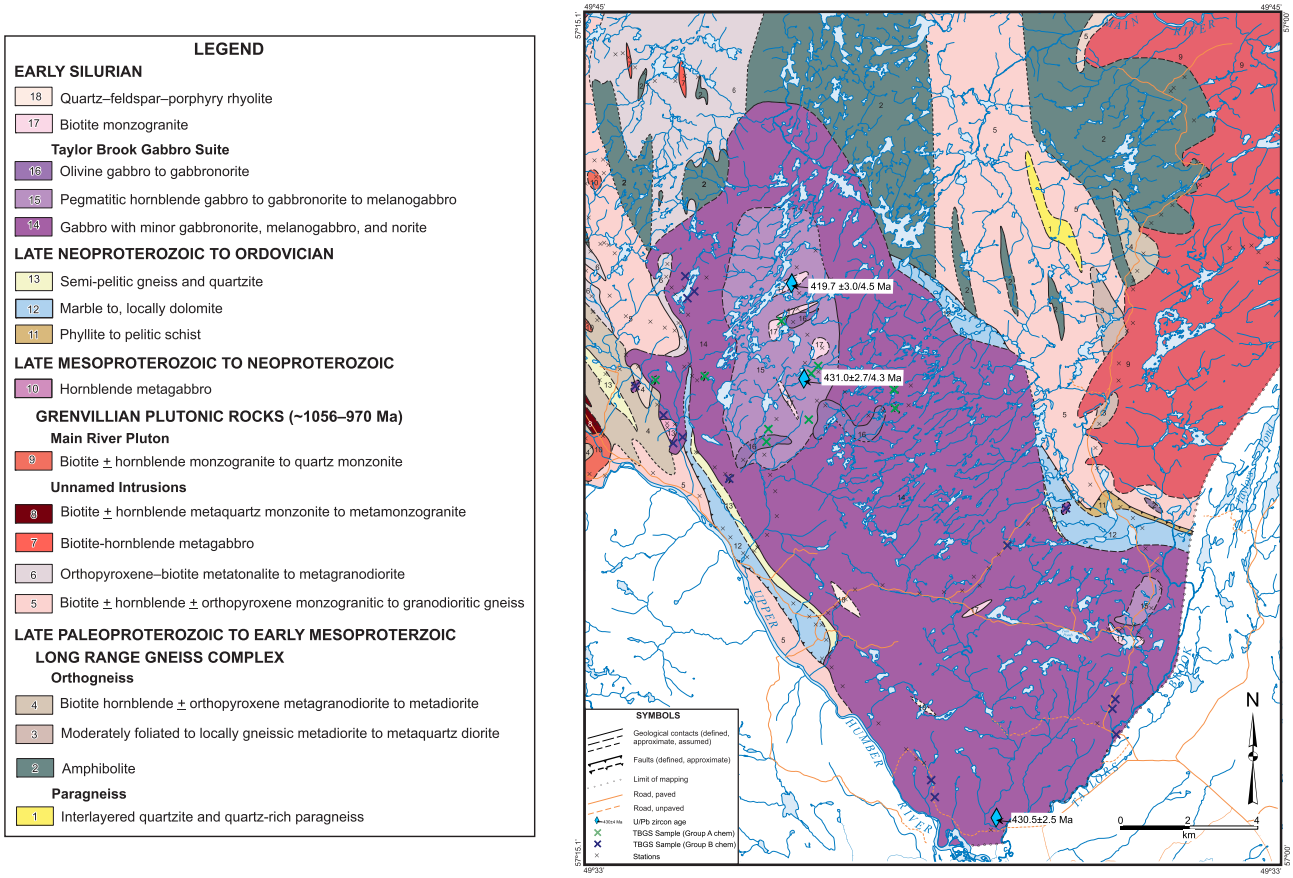

plemental material E. Major and trace element geochemical data are in supplemental material F. Isotopic data are presented in supplemental material G.

3.1. Silurian magmatism—field mapping and petrography

3.1.1. Taylor Brook Gabbro Suite (TBGS)

The northwest-oriented, oblong TBGS, mapped at a scale of 1:50 000, comprises three distinct phases: (1) a laterally extensive medium- to coarse-grained gabbro (unit 14: Fig. 2); (2) a coarse-grained to pegmatitic gabbro to melanogabbro (unit 15: Fig. 2), and; (3) a sporadically mappable phase of olivine gabbro to gabbronorite (unit 16: Fig. 2; Hinchey 2020). The most striking feature of the suite is its textural and compositional heterogeneity with abundant evidence of magma mingling (Fig. 3). Igneous layering is locally preserved (Figs. 3A and 3B), typically displaying moderate dips towards the centre of the body. However, the dip direction of this layering is not always consistent and locally dips outward. This may be the result of rotation associated with younger phases. The composite intrusion was originally termed the Taylor Brook Gabbro Complex (Owen 1991); however, Hinchey (2010) suggested renaming the intrusion to the TBGS as this would better reflect its compositional variability. Heaman et al. (2002) reported a physical abrasion, bulk zircon U–Pb zircon date of 430.5 ± 2.5 Ma from a fine-grained gabbro phase from the margin of the suite (Fig. 2). Because of its heterogeneity, it was questioned whether this age reflected the entirety of the TBGS, or if the Silurian age represented a younger, fine-grained mafic intrusion (Collins 2007).

Rocks of phase one (unit 14; Fig. 2) are medium- to coarse-grained, mesocratic gabbro and include minor gabbronorite, melanogabbro, and norite phases (Fig. 4). The unit is heterogeneous because of compositional variations at the centimetre scale. Along the margins of the intrusion, the gabbro is fine-grained. This phase typically preserves igneous layering and evidence for repetitive injection of magma and resultant magma mingling. Igneous layering varies from a few centimetres to a few metres in thickness and is highlighted by variations in grain size and mineralogy (Fig. 3B). Along the northwestern margin of the intrusion, the gabbro contains prominent flattened/compacted igneous layers occasionally defined by 2–10 cm thick discontinuous layers of massive magnetite (Fig. 3C). Locally spinel (hercynite)-rich layers define the igneous layering (Fig. 4B). This gabbroic phase has been intruded by medium-grained melanogabbro dykes that display chilled margins (Fig. 3C) and by other finer grained gabbroic dykes that are co-magmatic. Cognate and accidental xenoliths also occur. Dykes of leucocratic gabbro and locally clinopyroxenite are also found in the fine- and coarse-grained

Fig. 3. Field photographs. (A) Igneous layering in the TGBS, illustrating planar compositional changes from leucocratic hornblende gabbro to melanocratic pyroxene hornblende gabbro. Layering is offset by late (Acadian?) brittle faulting (09AH002). (B) Dm-scale igneous layering of leucogabbro, pyroxene–hornblende gabbro, plagioclase porphyritic layers, magnetite-rich layers (black), and spinel-rich layers cut by a fine-grade melanogabbro (09AH143). (C) Melanogabbro dyke with chilled margin cutting magnetite-rich layers alternating with plagioclase-enriched versus clinopyroxene-enriched layers. (D) Magma mixing textures between coarse-grained, homogenous gabbronorite and fine-grained melanogabbro. (E) Megacrystic gabbro that brecciated three other phases composed of coarse-grained melanogabbro, fine-grained black hornblende gabbro, and fine-grained melanogabbro (09AH308). (F) Pegmatitic to very coarse-grained gabbro to melanogabbro cut by dykelettes of fine-grained grey gabbro (09AH319). (G) Coarse-grained, homogenous gabbronorite with cumulate texture (09AH146). (H) Contact between fine-grained monzogranite with chilled margins against variably textured gabbro (09AH368). (I) Melanogabbro intruding a foliated granitic Grenvillian Pluton. (J) Gabbro with xenoliths of the Long Range Gneiss Complex. (K) Medium-grained, monzogranite (09AH303). (L) Quartz–feldspar porphyry rhyolite (09AH278). Mag, magnetite; Amp, Amphibole; F. gr., fine-grained; C. gr., coarse-grained; Opx, orthopyroxene; Cpx, clinopyroxene; LRGC, Long Range Gneiss Complex.

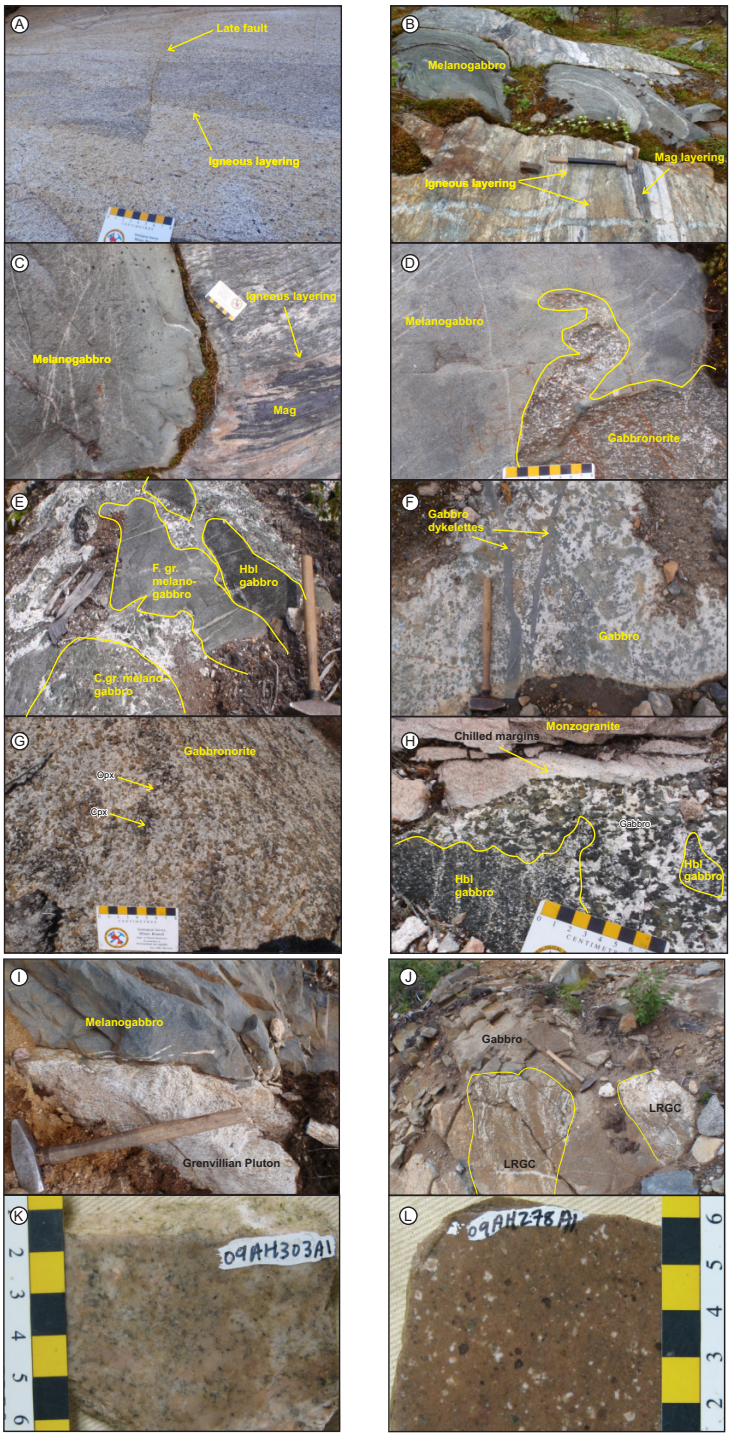

Fig. 4. Scanning electron microscopy-mineral liberation analysis images with semiquantitative weight percentages and photomicrographs of the samples. Top left, plane polarized light; bottom right, cross polarized light. (A) and (D) Olivine gabbro—Group A, (B) and (E) gabbro—Group B (hercynite-rich layer), and (C) and (F) pyroxene hornblende gabbro—Group B. Mag, magnetite; Opx, orthopyroxene; Pl, plagioclase; Hc, hercynite; Cpx, clinopyroxene; Ol, Olivine; Hbl, Hornblende.

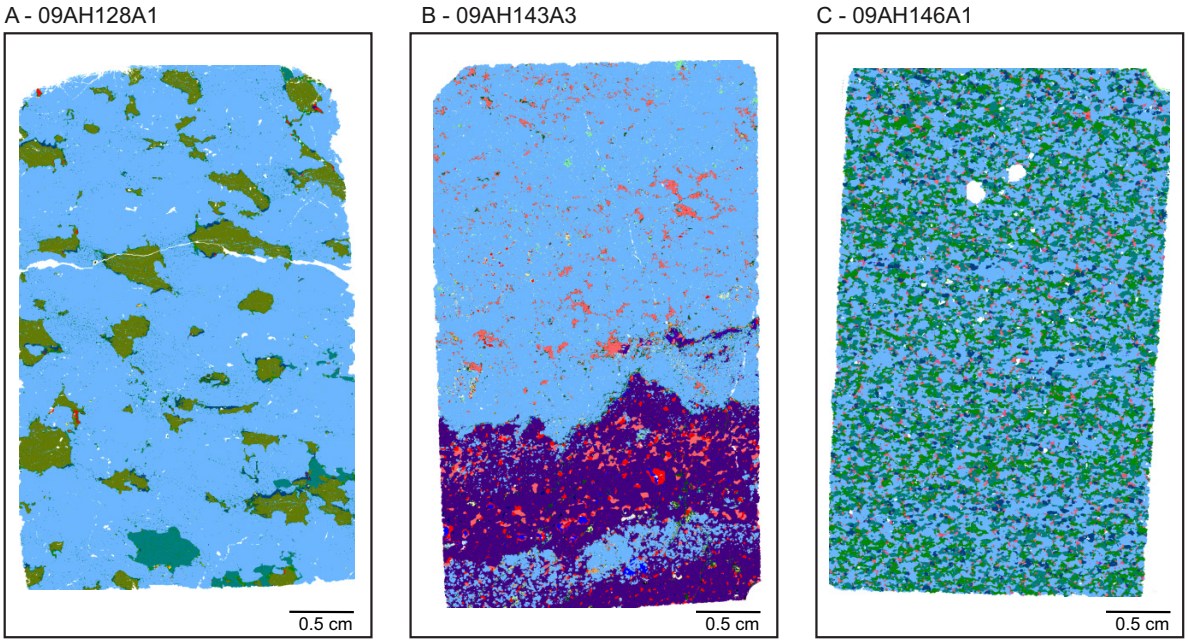

Weight Percentage(%)

Samples	09AH146A	09AH143A	09AH128A
Quartz	-	0.04	-
Plagioclase	78.26	54.39	41.20
Chlorite	0.36	1.89	0.08
Biotite	0.03	0.36	-
Muscovite\Sericite	0.01	0.81	-
K Feldspar	-	-	-
Calcite	-	0.01	-
Epidote	0.26	0.46	0.03
Hornblende-Fe	2.61	-	21.17
Rutile	-	0.01	-
Rutile-Ilm mix	0.01	0.35	0.13
Titanite	-	0.01	-
Apatite	-	-	0.41
Garnet	0.01	0.08	-
Clinopyroxene (Fe-Mg)	2.86	-	20.76
Orthopyroxene	1.66	-	6.87
Olivine	12.92	-	-
Serpentine	0.46	-	-
Allanite	0.08	-	0.06
Zircon	-	0.01	-
Chalcopyrite	0.01	–	0.03
Iron Oxide	0.30	3.99	0.33
Pyrite	-	0.03	-
Ilmenite	0.05	5.90	1.90
Ti-magnetite	0.03	0.47	6.99
Hercynite	0.02	29.42	0.02
Corundum	-	1.60	-
Unknown alteration	-	0.12	-
Pyrrhotite	0.04	-	-
Pentlandite	0.01	-	-

gabbro phases. Textures indicative of magma mingling between leucocratic and melanocratic phases are also apparent (Fig. 3D). Plagioclase porphyritic gabbroic dykes that have chilled margins crosscut all units and are interpreted to represent the final pulses of gabbroic plutonism. Cumulate textures are apparent in the coarser grained variants of this unit (supplemental material B). Minor occurrences of disseminated sulfides, primarily pyrite and chalcopyrite, and magnetite are scattered throughout the intrusive phase (Fig. 4 and supplemental material B).

The second major intrusive unit (unit 15) is medium- to coarse-grained to pegmatitic hornblende gabbro to gabbronorite to melanogabbro that outcrops in the northern part of the complex (Fig. 2) and cuts fine-grained grey gabbro and melanogabbro that likely represent unit 14 (Fig. 3E). Unit 15 contains pyroxene crystals up to 4 cm long. The pyroxene is typically subhedral with cumulate textures locally preserved. The gabbro and melanogabbro contain irregular patches that are enriched in plagioclase. Like the other intrusive phases, this phase locally contains minor iron and copper sulfide (pyrite, chalcopyrite) minerals and magnetite. Co-magmatic to late, fine-grained dykes of melanogabbro and locally clinopyroxenite 5–10 cm wide cut unit 15 (Fig. 3F).

The third mappable unit, olivine gabbro to gabbronorite (unit 16; Fig. 2), is coarse-grained (Fig. 3G) and occurs as small mappable bodies throughout the suite and also as outcrop-scale variations in unit 14. The unit preserves a cumulate texture and locally contains plagioclase-enriched patches (supplemental material B). Disseminated magnetite and sulfide minerals occur locally. The unit is crosscut by finer-grained dykes of co-magmatic gabbro and leucogabbro.

The TBGS is heterogeneous at all scales. The fluidity of the intrusive phases is indicated by syn-crystallization deformational features such as compacted igneous layering, dropped pendants that have disrupted igneous layers, magma mingling of leucocratic and melanocratic phases, multiple phases of non-chilled, irregular dyke emplacement, and commonly repeated rock compositions (Fig. 3H). Modal abundance of magnetite is highly variable, with some units containing 2–5 cm thick layers of massive magnetite to other phases that are virtually devoid of magnetite.

The TBGS represents a laccolithic intrusion that intruded the Long Range Inlier (Figs. 3I and 3J). It is interpreted to have utilized pre-existing crustal-scale discontinuities, likely precursors to the DVG system, as a conduit for the multiple pulses of magma (Hinchey 2010). Thus, rather than representing a massive batholith, it is possibly a thinner sheet-like, composite intrusion. This would explain the large aerial extent of this pluton (>175 km^2), which would otherwise have required a regionally extensive chamber to produce such a large batholith.

3.1.2. Silicic magmatism

Two phases of silicic magmatism are spatially associated with the TBGS (Hinchey 2010, 2020). One forms leucocratic biotite monzogranite (unit 17; Fig. 2) dykes and sills that are locally large enough to be mappable (1:50 000 scale). These bodies are generally northeast-trending, range from 10 to 100 m in thickness, and intrude the pegmatitic gabbro to melanogabbro. The monzogranite is medium-grained (Fig. 3K), contains pegmatite patches and preserves 2–3 cm wide chilled margins. The second phase of silicic magmatism is fine-grained quartz–feldspar porphyritic rhyolite dykes occurring in the southern portion of the intrusive suite (unit 18). These dykes are pink, have an aphanitic groundmass, and contain euhedral, 1–4 mm long quartz and alkali feldspar phenocrysts (Fig. 3L). Based on proximity, the silicic magmatism was suggested to be correlative with Silurian volcanic rocks of the Sops Arm Group, located east of the Long Range Inlier and the DVF system (Erdmer 1986).

4. U–Pb geochronology

When using U–Pb SHRIMP data of Paleozoic zircon, the generally accepted age to report is the ^{206}Pb/^{238}U age (Black et al. 2003). This is because the ^{207}Pb counts in young zircon are low and highly sensitive to the assumed common lead composition, leading to extremely large uncertainties in individual analyses. As a result, the ^{207}Pb/^{206}Pb age estimates carry significant uncertainty, rendering discordance calculations and their ages difficult to interpret. Typical data treatment for Phanerozoic zircon is to plot the results uncorrected for common Pb, without the additional common Pb correction uncertainty, on a Tera–Wasserburg diagram and evaluate its collinearity. The collinear data represent a single age population with varying degrees of common Pb.

4.1. Hornblende gabbro (09AH369A; GSC lab number 10144)

A sample from a very coarse-grained, cumulate-textured, hornblende gabbro from unit 14 was collected for analysis (Figs. 2, 5A, and 5B). In outcrop, the hornblende gabbro is compositionally heterogeneous and includes minor patches that grade into leucogabbro, gabbro, and norite. Amphibole comprises over 50% of the rock, with three distinct phases of growth. In the first phase, magnesio-hornblende replaces clinopyroxene. The second phase is subhedral pargasite. In the third phase, small acicular pargasite grains grow around the earlier pargasite (Figs. 5C and 5D).

The sample yielded abundant colourless to pale brown anhedral zircon (Fig. 6A). Some grains are prismatic and may rarely contain inclusions. In CL images, the grains are strongly luminescent and exhibit straight oscillatory zoning (supplemental material D).

A total of 25 zircon grains, varying in shape and internal structure, were analyzed. Thirty-two analyses resulted in ^{206}Pb/^{238}U dates (^{207}Pb-corrected) from 452 to 413 Ma with an additional 2 grains yielding Grenvillian ages (1102, 999 Ma; supplemental material C). All the grains, including the Grenvillian-aged ones, are characterized by low U (less than 100 ppm, most less than 50) and high Th/U (0.6–1.2). Both the anhedral/fragmental morphology and chemistry of the zircon grains are consistent with what is com-

Fig. 5. Field photographs (A and B) and photomicrographs (C and D) of the hornblende gabbro (09AH369A) collected for U–Pb zircon analysis. Field photographs (E and F) and photomicrographs (G and H) of the monzogranite (09AH368A) collected for U–Pb zircon analysis. Prg, pargasite; Mhb, magnesiohornblende; Qt, quarts; Kfs, potassium feldspar; Pl, plagioclase.

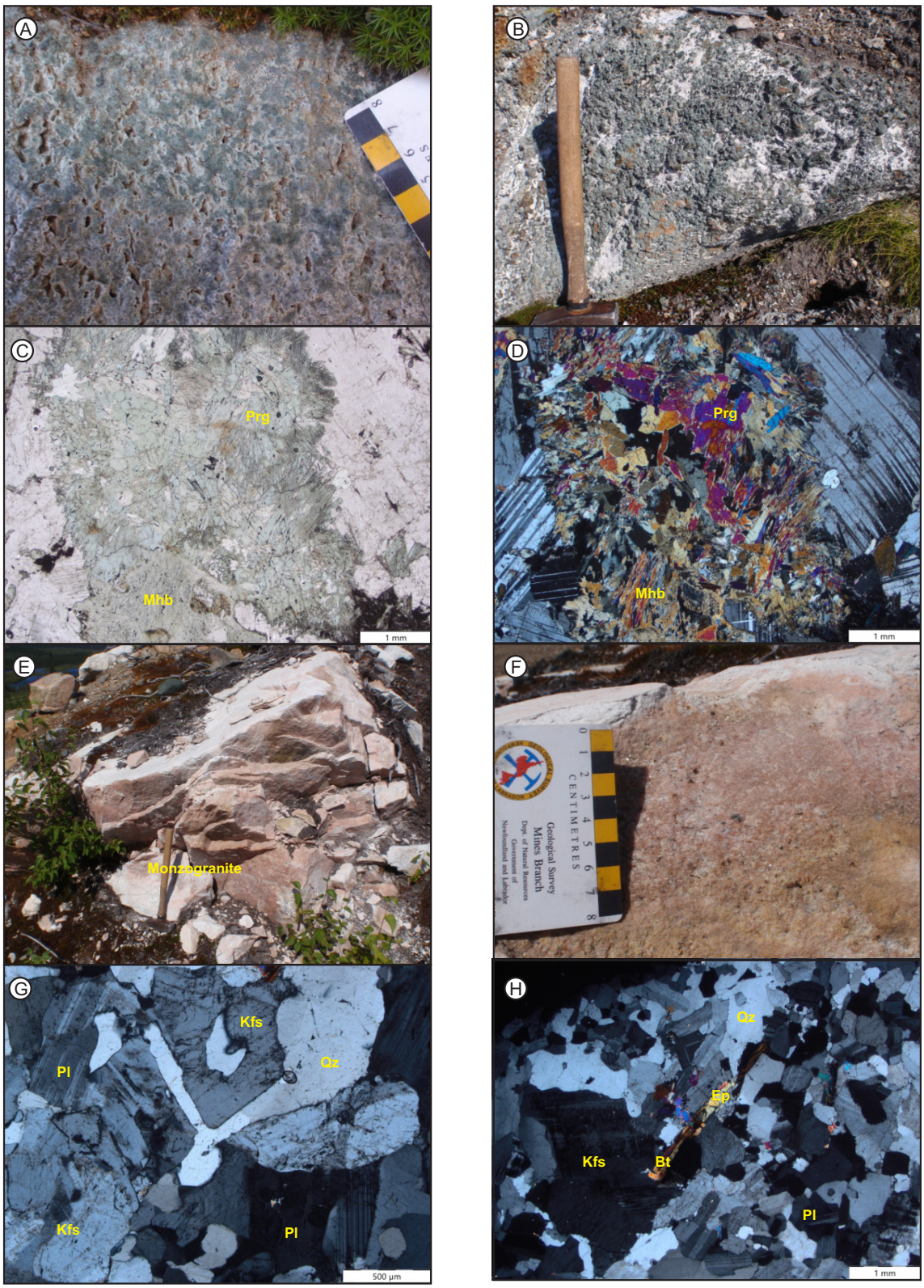

Fig. 6. Tera–Wasserburg concordia diagrams of U–Pb results from this study. Data plotted are uncorrected for common Pb, whereby the offset from the concordia curve is a reflection of the proportion of common Pb using the ^{207}Pb method. Ellipses shown in red are used in the calculation of the crystallization age, and grey ellipses are excluded. Data plotted at 95% confidence interval. The uncertainty on the interpreted age is reported as 2σ internal/external. (A) Results for hornblende gabbro sample 09AH369A (Geological Survey of Canada laboratory number 10144). Inset: transmitted light images of representative population of zircon grains. (B) Results for monzogranite sample 09AH368A (Geological Survey of Canada laboratory number 10146). Inset: transmitted light images of representative population of zircon grains.

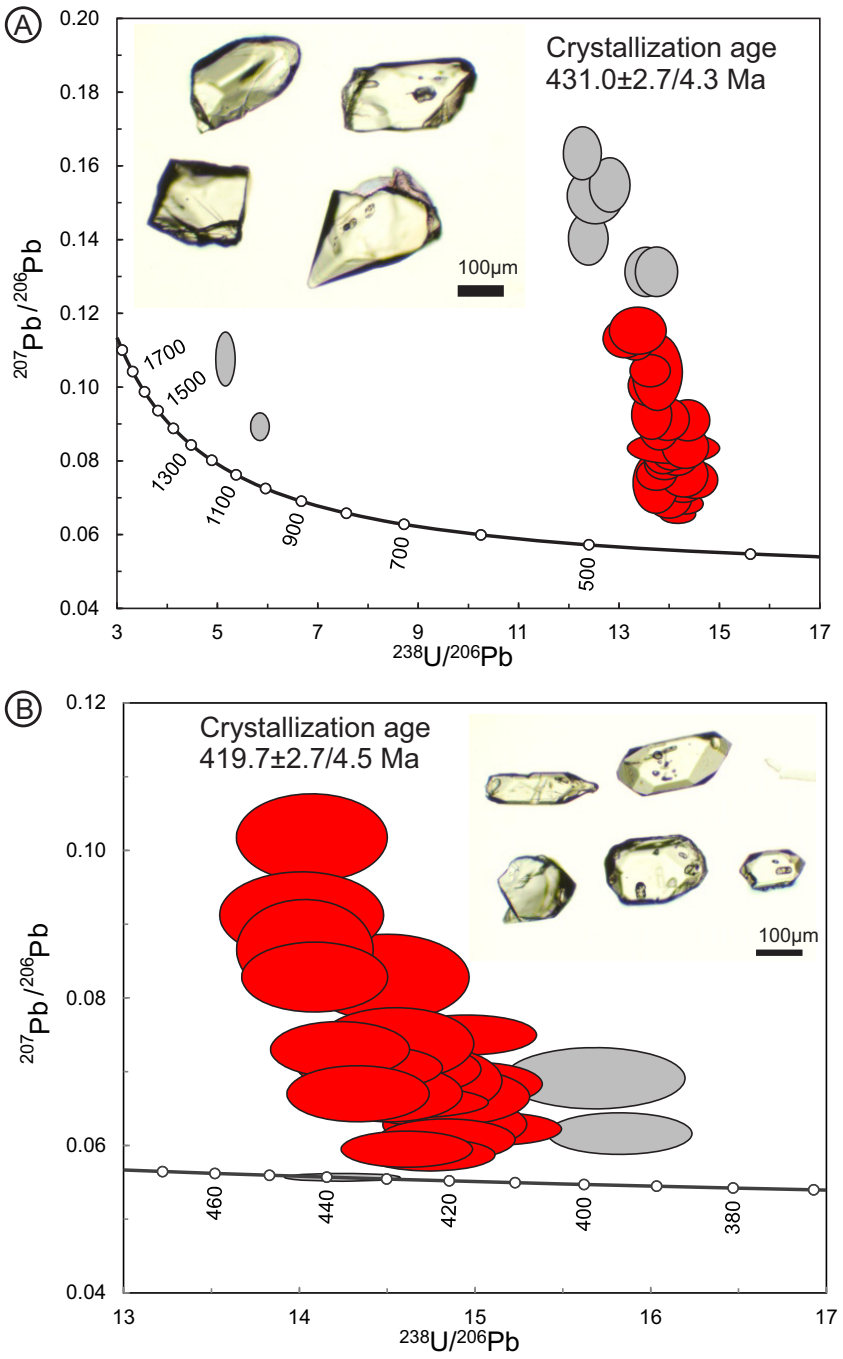

monly observed in mafic plutonic rocks (Heaman et al. 1990; Heaman and LeCheminant 1993). A weighted mean ^{206}Pb/^{238}U age of 431.0 ± 2.7/4.3 Ma (2σ uncertainties internal/external, ^{207}Pb-corrected, n = 26, mean square of weighted deviates (MSWD), = 1.3, probability of fit = 0.05) was calculated using analyses with the lowest common Pb (uncorrected ^{207}Pb/^{206}Pb < 0.12) to minimize the effect of the correction on the age (Fig. 6A). This is interpreted as the crystallization age of the hornblende gabbro. The Grenvillian age zircons are interpreted as inherited.

4.2. Monzogranite (09AH368A; GSC lab number 10146)

This sample is from a leucocratic, fine-grained, biotite monzogranite (unit 17; Figs. 2, 5E, and 5F) that cuts unit 15. In thin section, plagioclase, quartz, and potassium feldspar are predominant phases with muscovite, epidote, chlorite, biotite, and magnetite as accessory phases (Figs. 5G and 5H). Some plagioclase grains contain sericite alteration. Evidence for minor post-crystallization deformation includes deformed undulose extinction in interstitial quartz and irregular, crosscutting, plagioclase polysynthetic twinning.

Approximately 40 zircon grains were mounted. Most grains are sharply faceted ranging from equant and stubby prisms to elongate with aspect ratios of 4:1 (Fig. 6B). Fluid inclusions and inclusions of other minerals are common. Most grains are strongly luminescent in CL, consistent with relatively low U content but a small number of grains have poor CL response, suggesting high U or older ages (supplemental material S4).

A total of 24 analyses were carried out on 17 zircon grains with variable shapes and internal structures. Twenty analyses resulted in $^{206}Pb/^{238}U$ dates (^{207}Pb-corrected) from 392 to 437 Ma (supplemental material S3). These were all from relatively low U zircon (less than 200 ppm) with the exception of one high U grain (3500 ppm), which returned the oldest age. High U grains are known to return anomalously old ages due to matrix effects during sputtering (White and Ireland 2012) and thus this analysis will not be considered in further discussions. The weighted mean $^{206}Pb/^{238}U$ age of 21 analyses is 419.7 ± 3.0/4.5 Ma (2σ uncertainties internal/external, ^{207}Pb-corrected $n = 20$, MSWD = 1.9, probability of fit = 0.01), which is interpreted as the age of the monzogranite (Fig. 6B). Two analyses were excluded on statistical grounds using the "autoreject" function of Isoplot4.15 (Ludwig 2012). Additional analyses on the same grain fall within the igneous population, suggesting that these two slightly younger results may have been affected by Pb loss. A comparison of the ages and the internal uncertainties is only appropriate when comparing the monzogranite and the gabbro in this report since they were analyzed during the same analytical session. When comparing with other datasets, the external uncertainty must be used.

5. Mineral chemistry, whole-rock lithogeochemistry, and isotopic chemistry

Mineral chemical analyses of nine samples of the TBGS were completed (supplemental material E). Representative lithogeochemistry for 30 diverse samples of the TBGS, four samples of monzogranite, and two samples of rhyolite were analyzed (supplemental material F). Table 1 provides a summary of select major and trace element ratios. A subgroup of nine samples was subsequently analyzed for whole-rock Sr and Nd isotopic compositions (supplemental material G).

5.1. Mineral chemistry (TBGS)

Olivine grains are compositionally unzoned and uniform on the sample scale. The Mg# in olivine (Mg# = 100 × molecular MgO/MgO + FeO^T) ranges from 67.0 to 77.1, with an average of 72.4 (Fig. 7A). Except for one gabbro sample, plagioclase ranges from bytownite ($An_{75-41}Ab_{58-24}Or_{0-2}$) to oligoclase ($An_{39}Ab_{59}Or_2$; Fig. 7B). One sample plots in the albite field ($An_{1-2}Ab_{97-99}Or_1$), likely reflective of alteration. Clinopyroxene has variable compositions between samples, although samples do not show systematic zoning in individual grains. Samples plot in two distinct groups, regardless of rock type. One group straddles the diopside to augite boundary (Fig. 7C), whereas the second group plots in the augite field with $Wo_{30-50}En_{33-50}Fs_{20-25}$. The Mg# values of clinopyroxene range from 60.5 to 98.9. Orthopyroxene ranges from enstatite to ferrosilite (Fig. 7C) with $Wo_{1-4}En_{3-78}Fs_{37-76}$ and Mg# values ranging from 39.1 to 80.1. Amphiboles are part of the calcic group with Mg# values of 45.9–82.7, and can be further classified as ranging from Ti-rich pargasite to magnesian hornblende (supplemental material E). Accessory phases typically comprise rutile, spinel (hercynite), magnetite, and ilmenite (supplemental material B and E).

5.2. Major and trace element geochemistry

5.2.1. Taylor Brook Gabbro Suite

Based on their major and trace element chemistry, the TBGS samples ($n = 26$) form two distinct geochemical groups that largely correlate with the lithological units. Group A comprises samples from units 15 and 16 that primarily occur in the central body of the intrusion (Fig. 2). Group A has SiO_2 contents ranging from 45.6 to 49.3 wt.%, with Al_2O_3 from 18.1 to 22.7 wt.%, CaO from 9.3 to 13.8 wt.% and MgO from 5.3 to 12.3 wt.% (supplemental material F). Group A exhibits moderate to high Mg# (57–76) and low TiO_2 concentrations ranging from 0.2 to 0.6 wt.%, except for one sample that has 1.8 wt.% TiO_2. Group B in contrast has relatively lower SiO_2 (42.2–48.5 wt.%), Al_2O_3 (11.9–17.5 wt.%), CaO (6.9–13.5 wt.%), and MgO (4.1–8.4 wt.%). Group B samples are from unit 14 that comprises most of the areal extent of the intrusion. Group B rocks exhibit low to moderate Mg# (35–60) and high TiO_2 concentrations ranging from 1.6 to 3.9 wt.%. Various major and trace elements are plotted against Mg# (Fig. 8) to illustrate fractionation trends. Both Ni and Cr decrease with decreasing Mg# (not illustrated). Group A samples show a clear trend of being less fractionated compared to the more evolved compositions of Group B (Fig. 8). On a total alkali–silica classification diagram, both groups largely plot in the gabbro field (Fig. 9A). However, the distinction between the less fractionated Group A samples from the more evolved Group B is illustrated on a Jensen cation plot (Fig. 9B).

Primitive mantle normalized (Sun and McDonough 1989) incompatible multi-element profiles of Group A rocks (Fig. 10A) are characterized by a slight enrichment in incompatible elements relative to primitive mantle, with concave-down to fractionated light rare earth element profiles (LREE; $(La/Sm)_{pm}$ = 0.50–2.2; the subscript pm refers to primitive mantle normalized values). In addition, the

Table 1.

Sample name	09AH303A	09AH308B	09AH321B	09AH368A	09AH278A	09AH410A	09AH128A	09AH143A	09AH161A	09AH163B	09AH164A	09AH257A	09AH273A	09AH293B	09AH297A	09AH316A	09AH319A	09AH346B	09AH347A	09AH352A	09AH399A	09AH276A	09AH304A	09AH002A	09AH275A	09AH369A	09AH323A	09AH324A	09AH396A	09AH158C	09AH133A	09AH146A
Lithology	Monzogranite	Monzogranite	Monzogranite	Monzogranite	qf Porphyry	qf Porphyry	Gabbro	Gabbro	Gabbro	Gabbro	Gabbro	Gabbro	Gabbro	Gabbro	Gabbro	Gabbro	Gabbro	Gabbro	Gabbro	Gabbro	Gabbro	Gabbronorite	Gabbronorite	Hbl gabbro	Hbl gabbro	Hbl gabbro	Ol gabbro	Ol gabbro	Cpx norite	Opx gabbro	Px Hbl gabbro	Ol gabbro
Unit	17	17	17	17	18	18	14	14	14	14	14	14	14	14	14	16	16	14	14	14	14	14	16	14	14	16	16	15	14	14	14	14
Group	Silicic	Silicic	Silicic	Silicic	Silicic	Silicic	B	B	B	B	A	B	B	B	B	A	A	B	B	A	A	B	A	B	B	A	A	A	A	B	B	A
Al_2O_3/Na_2O	3.4	3.5	3.2	3.4	3.0	3.0	7.0	5.7	5.3	4.2	6.7	4.9	3.7	19.5	4.2	6.7	7.2	5.3	3.0	6.9	7.8	5.2	5.5	4.5	3.8	6.3	6.8	7.8	9.6	5.1	5.9	7.6
$(La/Yb)_{pm}$[a]	2.7	7.6	3.8	2.7	3.8	1.7	2.4	9.8	1.9	7.6	2.2	4.5	5.8	5.0	3.9	2.2	1.9	2.1	4.1	5.0	2.8	3.5	2.9	6.2	4.9	3.2	1.0	2.1	1.1	3.6	2.1	2.6
Al_2O_3/TiO_2	227.8	148.4	224.2	203.1	223.3	236.9	6.2	5.2	7.5	3.4	37.4	9.8	5.5	8.6	4.9	62.3	77.3	9.9	7.8	49.3	107.9	9.6	11.1	8.4	4.2	35.1	36.1	35.7	48.0	3.1	11.1	73.5
Ti/Sc	102.3	291.4	167.1	191.1	48.5	40.8	263.9	514.6	189.3	644.3	88.4	349.4	567.8	479.9	549.3	89.1	102.0	263.6	363.5	191.8	82.1	312.5	656.8	457.6	552.7	262.1	67.5	240.4	66.2	472.5	257.6	118.8
Ti/Yb	167.2	495.6	140.3	252.3	124.6	95.1	4272.4	5246.7	1782.8	7346.8	3403.8	2885.3	3280.1	3625.2	3455.6	3777.1	4104.5	3283.4	3683.4	2959.5	4126.3	3575.7	13766.5	3982.2	4321.9	4603.6	3007.3	7648.9	3897.8	5169.3	3348.8	4623.1
$(Ti/Zr)_{pm}$[a]	0.07	0.03	0.04	0.09	0.04	0.03	1.17	1.92	0.59	0.88	1.18	0.49	0.18	0.52	0.72	1.29	1.69	0.57	0.51	0.68	1.39	0.62	2.49	0.52	0.47	1.93	1.30	2.08	1.61	0.60	0.60	2.20
$(Nb/La)_{pm}$a	3.2	2.7	1.3	5.7	2.7	5.6	0.9	0.5	0.8	0.9		0.6	0.6	0.8	0.5			0.6	0.5	0.4		0.5	1.2	0.5	0.6					1.7	0.5	
$(Nb/Th)_{pm}$[a]	0.5	0.4	0.4	0.5	0.2	0.2		2.8	6.0	3.6		2.6	2.4	0.3	0.8			1.0	0.7	0.8		0.8		1.3	2.0					8.9	0.9	
Nb/Y	1.3	2.8	0.6	3.1	0.9	1.0	0.2	0.4	0.2	0.6		0.3	0.3	0.4	0.2			0.1	0.2	0.2		0.2	0.4	0.3	0.3					0.6	0.1	
Nb/U	8.0	15.6	10.0	13.3	3.1	12.1		95.0		120.0		110.0	40.0	3.6	24.0			20.0	16.0			20.0		50.0	50.0					150.0	30.0	
Nb/Yb	9.5	22.7	5.6	17.5	11.3	10.8	2.5	5.1	1.8	7.5		3.0	3.8	4.5	2.2			1.3	2.4	2.2		2.0	3.8	3.3	3.1					6.7	1.1	
Nb/Ta	9.5	10.4	8.2	9.0	8.7	8.9	16.0	19.0	20.0	15.0		18.3	16.7	21.7	13.3			13.3	16.0			20.0	15.0	14.3	15.0					15.8	15.0	
Zr/Y	2.9	11.4	3.4	5.8	1.8	1.7	3.0	1.6	2.2	5.5	2.4	5.4	7.9	5.1	3.6	2.0	1.6	4.5	5.7	4.8	2.7	4.5	4.6	6.6	4.9	2.3	1.7	2.6	2.2	6.6	4.9	2.0
Zr/Nb	2.4	4.1	6.0	1.9	1.9	1.8	12.8	4.6	10.9	9.0		17.2	23.7	12.5	17.8			37.0	25.1	21.5		22.7	12.3	19.7	17.5					10.9	45.3	
Zr/Sc	13.7	55.1	40.0	24.6	8.4	8.1	2.0	2.3	2.1	5.9	0.6	6.2	15.5	7.4	6.3	0.6	0.5	3.8	6.0	3.1	0.5	4.0	2.2	7.5	7.0	1.5	0.4	1.0	0.4	6.7	3.7	0.5
Hf/Sm	1.9	3.2	1.5	3.7	0.7	0.8	0.6	0.1	0.5	0.6	0.5	0.7	0.8	0.6	0.6	0.5	0.5	0.8	0.8	0.6	0.4	0.7	0.8	0.8	0.6	0.3	0.6	0.7	0.4	0.8	0.8	0.5
$(Hf/Sm)_{pm}$[a]	2.8	4.6	2.2	5.3	1.0	1.1	0.8	0.2	0.8	0.9	0.8	1.0	1.1	0.9	0.8	0.7	0.7	1.1	1.1	0.9	0.6	1.0	1.2	1.2	0.9	0.5	0.8	1.0	0.6	1.2	1.2	0.7
$(La/Sm)_{pm}$[a]	3.3	5.8	3.0	4.3	1.7	0.9	1.1	1.8	1.4	2.1	1.2	1.8	1.9	1.7	1.6	1.0	0.9	1.0	1.7	2.2	1.2	1.4	1.5	2.4	1.8	1.2	0.6	1.0	0.5	1.3	1.1	1.2
$(Sm/Yb)_{pm}$[d]	0.6	1.0	1.0	0.5	1.7	1.5	1.7	4.3	1.0	2.8	1.4	1.9	2.4	2.2	1.9	1.8	1.7	1.6	1.8	1.7	1.9	1.9	1.5	2.0	2.1	2.1	1.3	1.7	1.7	2.1	1.5	1.7
$(Ta/U)_{pm}$[a]	0.4	0.8	0.6	0.8	0.2	0.7		2.6		4.1		3.1	1.2	0.1	0.9			0.8	0.5			0.5		1.8	1.7					4.9	1.0	
Zr/Hf	20.4	32.2	24.7	20.0	20.3	18.9	37.8	45.8	38.9	45.0	36.7	45.0	52.7	46.6	41.8	30.0	26.7	44.8	47.9	47.8	40.0	38.9	41.1	44.8	45.2	42.0	27.1	32.5	32.5	46.2	45.3	26.7
Sc/Y	0.2	0.2	0.1	0.2	0.2	0.2	1.5	0.7	1.1	0.9	3.9	0.9	0.5	0.7	0.6	3.5	3.2	1.2	1.0	1.5	5.0	1.1	2.1	0.9	0.7	1.6	4.0	2.5	5.9	1.0	1.3	3.9
deltaNb[b]	0.9	0.2	0.5	0.8	1.2	1.3	0.2	0.9	0.4	0.1				0.0	0.0							-0.2	0.0		-0.1							
Zr/Ti	0.1	0.2	0.2	0.1	0.2	0.2	0.0	0.0	0.0	0.0	0.0	0.0	0.0	0.0	0.0	0.0	0.0		0.0	0.0	0.0	0.0	0.0	0.0	0.0	0.0	0.0	0.0	0.0	0.0	0.0	0.0
$(La/Yb)_{cn}$[c]	2.1	5.9	2.9	2.1	2.9	1.3	1.8	7.5	1.5	5.9	1.7	3.5	4.5	3.9	3.0	1.7	1.4	1.6	3.2	3.8	2.2	2.7	2.2	4.8	3.8	2.5	0.8	1.6	0.8	2.8	1.6	2.0
Eu/Eu*[d]	0.4	0.9	0.4	0.7	0.2	0.1	1.0	0.9	0.9	1.2	1.6	1.0	0.9	0.9	0.8	2.0	2.1	1.0	1.0	1.6	2.2	1.0	2.0	1.1	0.9	1.5	1.4	2.1	1.4	0.9	1.1	2.1
Y/Ti	0.0	0.0	0.1	0.0	0.1	0.2	0.0	0.0	0.0	0.0	0.0	0.0	0.0	0.0	0.0	0.0	0.0	0.0	0.0	0.0	0.0	0.0	0.0	0.0	0.0	0.0	0.0	0.0	0.0	0.0	0.0	0.0
$(Tb/Yb)_{cn}$[c]	0.7	0.9	0.9	0.6	1.6	1.4	1.5	2.5	1.0	1.9	1.6	1.4	1.8	1.6	1.6	1.9	1.2	1.5	1.6	1.6	1.6	1.4	1.2	1.4	1.7	1.8	1.4	1.2	1.6	1.7	1.3	1.2
Mg#[e]	30.7	32.5	34.4	31.2	28.9	23.6	40.3	37.5	44.9	37.0	69.9	53.8	36.8	58.6	38.2	69.1	72.6	55.4	50.4	66.9	72.7	57.2	56.9	49.2	35.5	62.7	73.3	70.4	76.4	35.1	59.6	68.9

[a]pm = primitive mantle normalized (Sun and McDonough 1989).
[b]ΔNb = log (Nb/Y) + 1.74 – 1.92 log (Zr/Y) (Fitton et al. 1997).
[c]cn = chondrite normalized (Sun and McDonough 1989).
[d]$Eu/Eu^* = Eu_{pm}/(GD_{pm} \times Sm_{pm})^{0.5}$.
[e]Mg# = ((MgO/40.312)/((MgO/40.312) + (FeOT/71.847)))*100.

Fig. 7. (A) Mg# in olivine versus NiO wt.% content. (B) Classification triangle for feldspar. (C) Wo–En–Fs ternary diagram for pyroxene (Morimoto 1988). Cpx, clinopyroxene; Ol, olivine; Hbl, hornblende; Opx, orthopyroxene.

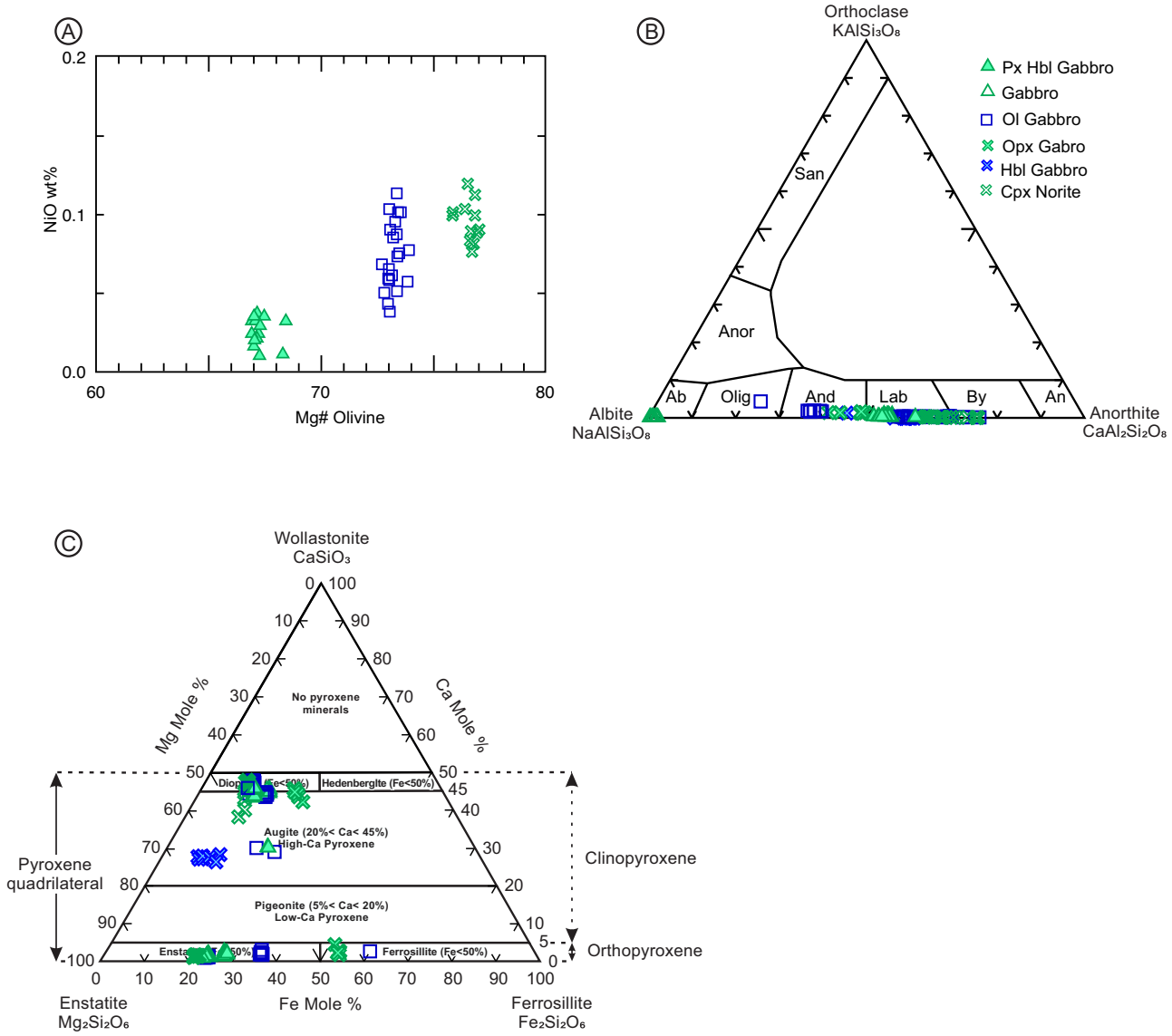

group displays variable multi-element profiles with flat to slightly fractionated heavy-rare earth element (HREE) profiles ($(Sm/Yb)_{pm}$ = 1.33–2.1), and variably positive to negative Zr and Ti anomalies and consistently positive Eu anomalies. On chondrite normalized REE diagrams, Group A shows flat to moderately steep slopes ($(La/Yb)_{cn}$ = 0.8–3.8; the subscript cn refers to chondrite normalized values; Sun and McDonough 1989) and strong positive Eu anomalies (Eu/Eu^*= 1.4–2.2; Fig. 10B). In comparison, Group B is significantly enriched in all incompatible elements relative to primitive mantle and to Group A, displaying flat to fractionated LREE ($(La/Sm)_{pm}$ = 1.0–2.4). The group also displays flat to strongly fractionated HREE profiles ($(Sm/Yb)_{pm}$ = 1.0–4.3) with predominantly positive Zr anomalies and an absence of Eu anomalies (Fig. 10C). On REE diagrams, Group B shows flat to moderately steep slopes and negligible Eu anomalies (Eu/Eu^* = 0.8–1.2; Fig. 10D), and typically shows stronger degrees of REE fractionation ($(La/Yb)_{cn}$ = 1.0–7.5).

5.2.2. Silicic samples

Four monzogranite and two rhyolite samples have similar geochemistry and will be treated as one group. They have narrow ranges of SiO_2 (75.5–76.0 wt.%), Al_2O_3 (13.1–14.0 wt.%), and Na_2O (3.9–4.6 wt.%) concentrations and plot as rhyolites on a total alkali–silica classification diagram (Fig. 9A). On a Jensen cation plot, the samples plot in the granite field (Fig. 9B). The samples plot as magnesian, metaluminous, and alkali calcic in composition (Fig. 9C). They have variable Zr/Nb (1.8–6.0) and Zr/Y (1.7–11.4) and high Al_2O_3/TiO_2 ratios (148.4–236.9; Table 1).

Primitive mantle normalized incompatible multi-element profiles of the samples (Fig. 10E) are enriched in all incompatible elements relative to primitive mantle, with moderate to strongly fractionated LREE ($(La/Sm)_{pm}$ = 0.9–5.8). In addition, the samples have flat to moderately fractionated HREE profiles ($(Sm/Yb)_{pm}$ = 0.5–1.7), Nb depletion relative to Th ($(Nb/Th)_{pm}$ = 0.2–0.5; Table 1), and Nb peaks relative

Fig. 8. Element, element ratios, or trace elements versus Mg# diagrams: (A) SiO_2 wt.%, (B) Co ppm, (C) Al_2O_3 wt.%, (D) Sr/Y, (E) Sc ppm, (F) CaO/Al_2O_3, (G) V/Ti, (H) Ti/Zr, and (I) Dy/Yb.

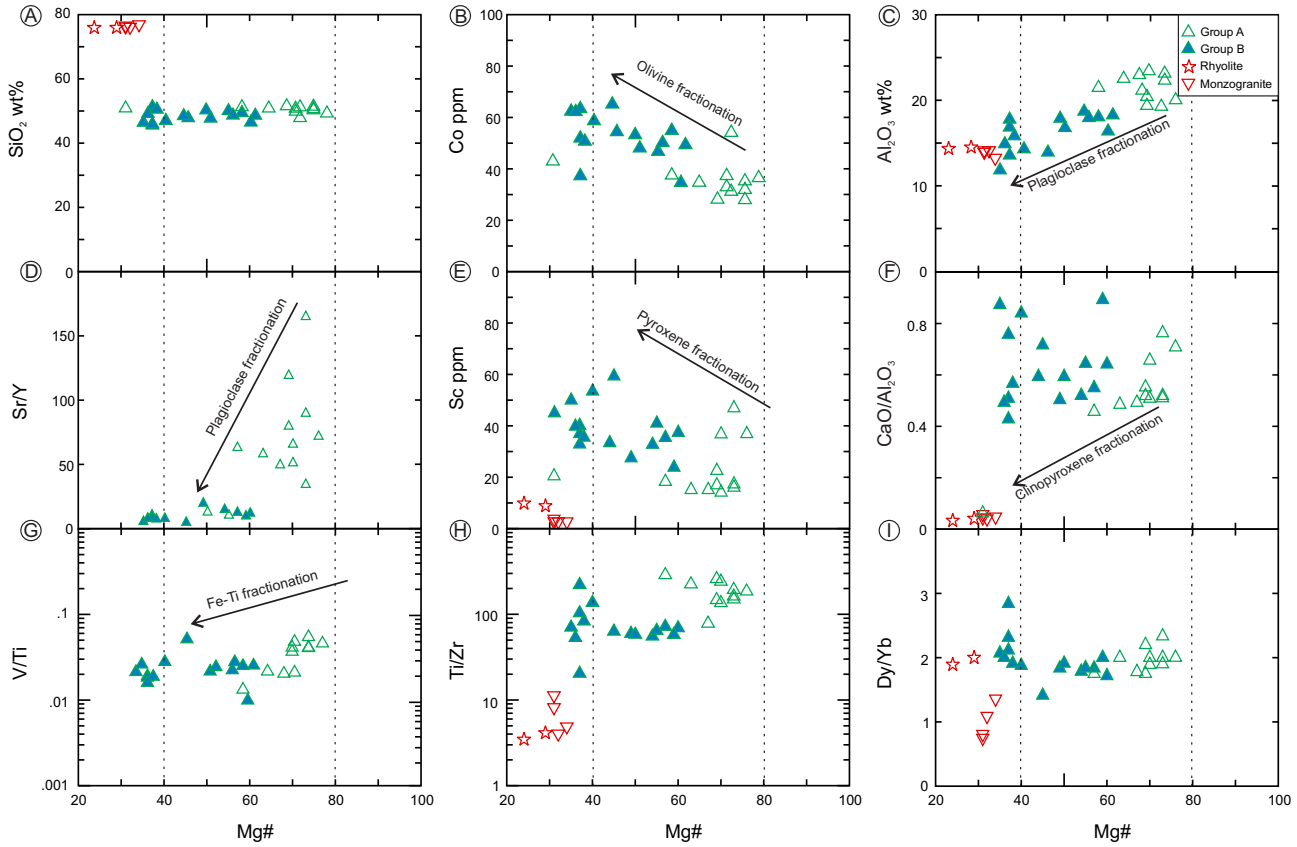

to La ($(Nb/La)_{pm}$ = 1.3–5.7; Table 1). They have ΔNb values that range from 0.2 to 1.2 (Table 1). On chondrite normalized REE diagrams, the samples are characterized by moderate REE fractionation ($(La/Yb)_{cn}$ = 1.3–5.9), and have moderate to strong negative Eu anomalies (Eu/Eu^* = 0.1–0.9; Fig. 10F).

5.3. Sr and Nd isotopic chemistry

Samples of TBGS and silicic rocks were analyzed for whole-rock Sr and Nd isotopes (supplemental material G). Not all samples yielded Sr isotopic ratios. Initial epsilon Nd and $^{87}Sr/^{86}Sr$ values were calculated using an age of 430 Ma. The initial $^{87}Sr/^{86}Sr$ ratios of Group A gabbros range from 0.703373 to 0.703887; Group B samples range from 0.702177 to 0.708250, and the silicic rocks range from 0.702124 to 0.713472. The Group A samples $^{143}Nd/^{144}Nd$ range from 0.512642 to 0.512858 with corresponding $\varepsilon Nd_{(t = 430\ Ma)}$ = +1.3 to +4.3. The Group B samples have $^{143}Nd/^{144}Nd$ that range from 0.511 944 to 0.512 915 and corresponding $\varepsilon Nd_{(t = 430\ Ma)}$ values that range from −8.6 to +6.4. The silicic samples have $^{143}Nd/^{144}Nd$ ranging from 0.512320 to 0.512612 and $\varepsilon Nd_{(t = 430\ Ma)}$ values that range from −3.7 to −0.7. The depleted mantle εNd value at 430 Ma is +9.32 (Goldstein et al. 1984) or +7.26 (DePaolo 1988). The range in $\varepsilon Nd_{(t = 430\ Ma)}$ values for all of the samples could indicate that they were derived from a LREE-enriched mantle source, or that they have experienced variable amounts of lithospheric contamination.

6. Discussion

6.1. Petrogenesis of the TBGS

6.1.1. Crustal contamination and crystal fractionation

The TBGS samples have relatively low LOI values (supplemental material F; LOI = 0.31–2.22 wt.%) and rarely have visible alteration in petrographic analysis. This indicates that post-emplacement changes in the geochemical signatures are unlikely. The TBGS contains low SiO_2 coupled with high MgO, $Fe_2O_3{}^T$, Cr, and Ni, indicating that the magma was derived from a mantle source. Mantle-derived magmas can be prone to crustal contamination, leading to an increase in incompatible elements like Th, Pb, La, Ce, Zr, LREE, and Hf and a decrease in Nb–Ta in derivative magmas (Sun and McDonough 1989; Rudnick and Gao 2003). Neither gabbro group of the TBGS exhibits marked increases in the incompatible elements nor a prominent Nb anomaly, suggesting that crustal contamination did not play a significant role in the formation of the TBGS (Fig. 10). However, the TBGS intrudes Grenvillian basement rocks that have strongly negative εNd_t values (Dickin 2004), and TBGS samples plot between the depleted mantle and the basement rocks, suggesting minor contamination by older continental lithosphere (Fig. 11). This is consistent with the minor amount of Grenvillian zircon inheritance observed in the U–Pb results (supplemental material

Fig. 9. Major-element plots for Silurian magmatism. (A) SiO_2 versus Na_2O/K_2O (Middlemost 1994). (B) Jensen cation plot (Jensen 1976). (C) SiO_2 versus modified alkali lime index ($Na_2O + K_2O$-CaO) (Frost and Frost 2008). TBGS, Taylor Brook Gabbro Suite.

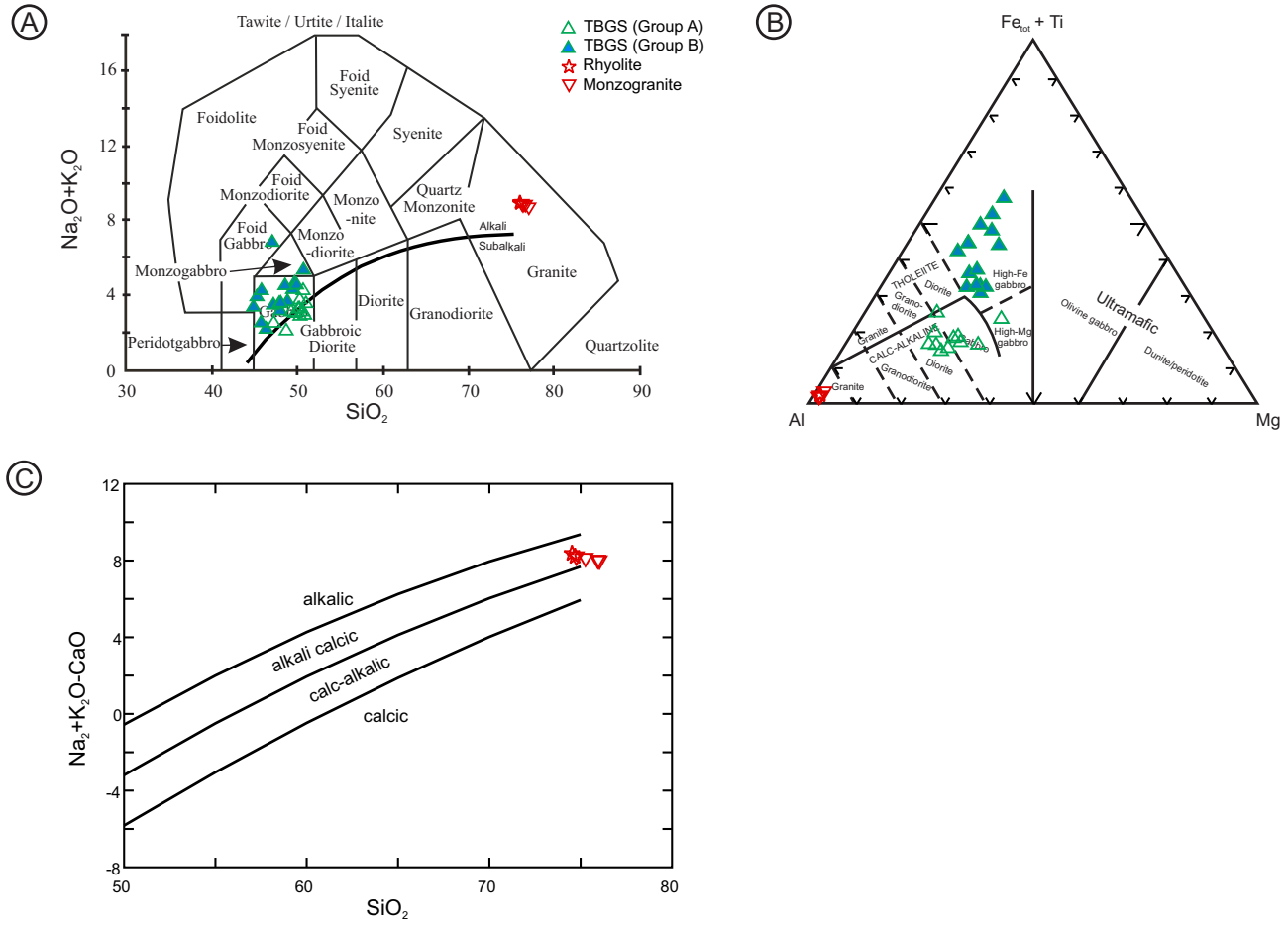

S3). As Sm and Nd are incompatible elements and more abundant in crustal rocks than in the mantle, even minor contamination of a mantle melt by older continental lithosphere will disproportionately control the εNd and model ages of the mantle-derived melts (Moyen et al. 2021).

The TBGS displays a range of textures from adcumulate to orthocumulate. These cumulate textures result from solid–liquid separation processes, as indicated by modal and grain-size layering at scales ranging from millimetres to decimeters (Fig. 4 and supplemental material B). Such textures suggest fractional crystallization/accumulation as the primary differentiation mechanism of the magmas. Therefore, the variation in the major and trace element composition of the rocks is largely controlled by the cumulate phases. SiO_2 varies little, whereas Co exhibits a negative correlation with Mg#, indicative of olivine fractionation (Figs. 8A and 8B). Plagioclase is the predominant cumulate mineral in Group A rocks, and their whole-rock Al_2O_3 contents reflect the effects of early plagioclase fractionation or accumulation under reducing conditions, where Fe^{2+} is stable in melt favouring plagioclase crystallization (Fig. 8C). A consistently strong positive Eu anomaly also highlights the cumulate nature of this group (Fig. 10B). In contrast, negligible Eu anomalies in the Group B samples suggest a shift in redox conditions from reducing to oxidizing, leading to the stabilization of Eu^{3+} (Fig. 9D; Terakado and Fujitani 1995; Cicconi et al. 2021). Alternatively, changes in fractional crystallization could also influence the stability of Eu^{3+} (Holder et al. 2020). Similarly, the Eu troughs in the silicic samples suggest that plagioclase removal likely influenced their compositions (Fig. 10F). The impact of plagioclase fractionation can be seen in trace element ratio diagrams (Fig. 8). The accumulation of plagioclase and the positive Eu anomalies in Group A rocks are indicative of low H_2O contents in the melts, as high H_2O contents can inhibit plagioclase accumulation (Müntener et al. 2001). In Fig. 8D, the Sr/Y trend is largely attributed to plagioclase accumulation in the cumulate Group A samples. The negative correlation of Mg# and Sc and CaO/Al_2O_3 supports pyroxene fractionation (Figs. 8E and 8F). The Fe–Ti oxides (magnetite and ilmenite) are also major phases in the gabbroic rocks, and their crystallization strongly influences the whole-rock FeO and TiO_2 contents of TBGS (Figs. 8G and 8H). As Zr appears to be controlled almost entirely by fractionation, increasing Ti/Zr ratio indicates the accumulation of ilmenite/titanite (Fig. 8H). The TBGS rocks display consistent Dy/Yb ratios, indicating insignificant amphibole fractionation (Fig. 8I). This is also supported by the amphibole mineral chemistry classifying almost exclusively as pargasite (supplemental material S5).

Fig. 10. Primitive mantle normalized multi-element plot for the Group A samples (A) and chondrite normalized REE diagram (B). Primitive mantle normalized (C) and chondrite normalized diagram (D) for Group B samples. Primitive mantle normalized (E) and chondrite normalized diagram (F) for silicic samples. Normalization values from Sun and McDonough (1989). On all subsequent figures: normal mid-ocean ridge basalt (N-MORB), enriched mid-ocean ridge basalt (E-MORB), and ocean-island basalt (OIB) data from Sun and McDonough (1989). Backarc basin basalt (BAB) from Ewart et al. (1998). Island arc tholeiite (IAT) and calc-alkaline basalt (CAB) from Stolz et al. (1990).

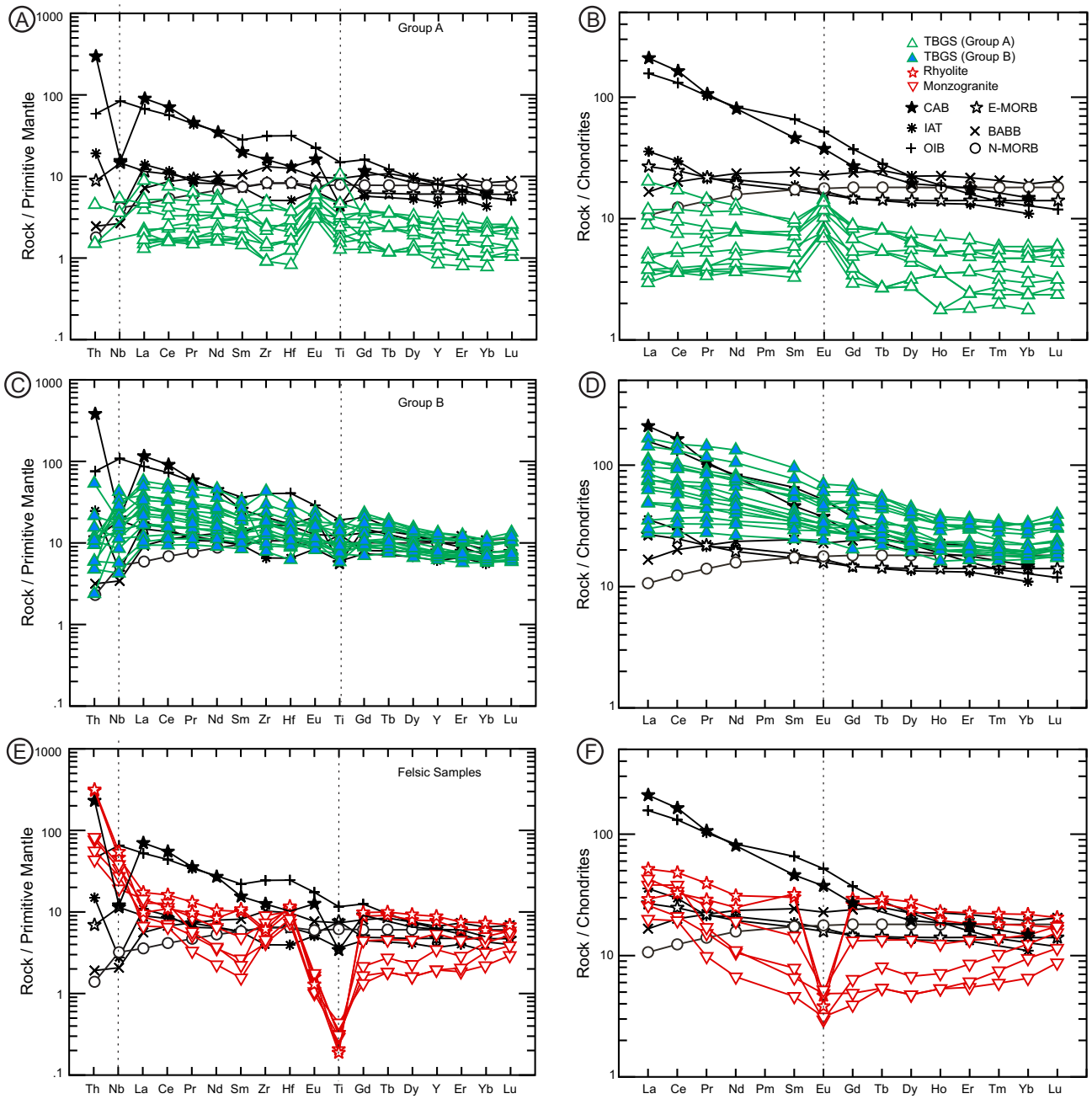

Concentrations of incompatible elements, such as La, Sm, and Yb, typically vary significantly during partial melting due to their preferential incorporation into the melt. In contrast, these elements show less variation during fractional crystallization, as they remain relatively enriched in the melt while the crystallizing mineral phases primarily exclude them. The TBGS samples show increasing La/Sm and La/Yb as La content increases (Figs. 12A and 12B), indicating progressive incompatible element enrichment during magmatic differentiation, supporting the role of fractional crystallization of the magma.

6.1.2. Mantle source components

Mantle source components of the TBGS can be interpreted using incompatible trace element ratios that are relatively

Fig. 11. (A) $^{147}Sm/^{144}Nd$ versus $\varepsilon Nd_{(t)}$. (B) $^{87}Sr/^{86}Sr_{(i)}$ versus $\varepsilon Nd_{(t)}$. CHUR—chondritic uniform reservoir. DM—depleted mantle (values calculated according to DePaolo 1988). The field for Grenvillian basement rocks from the Long Range Inlier is from Dickin (2004). Mantle array inferred at 430 Ma. TBGS, Taylor Brook Gabbro Suite.

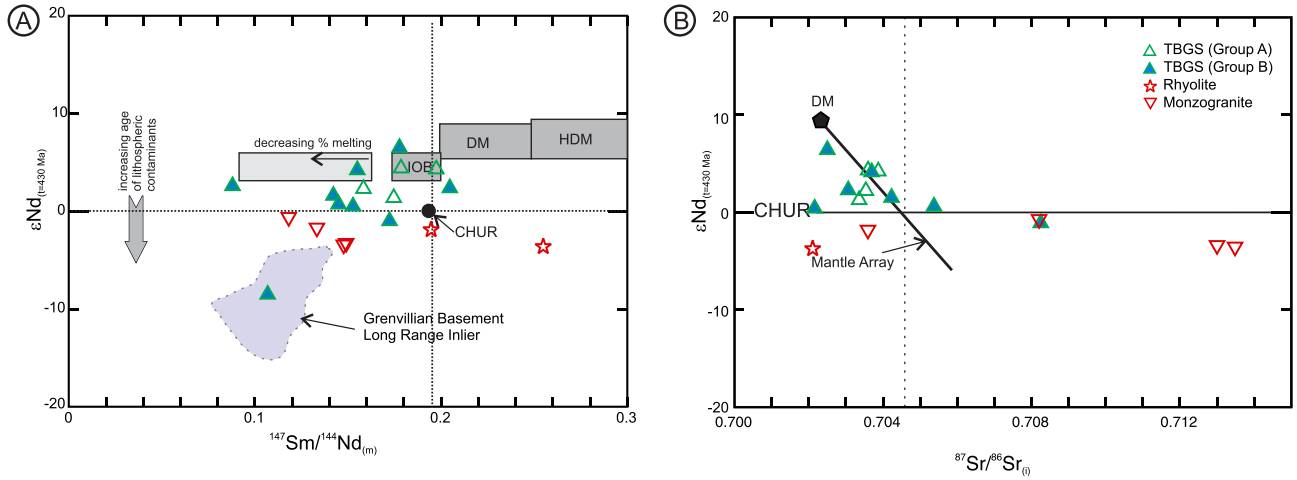

Fig. 12. Discrimination diagrams (A) La versus La/Sm. (B) La versus La/Yb. TBGS, Taylor Brook Gabbro Suite.

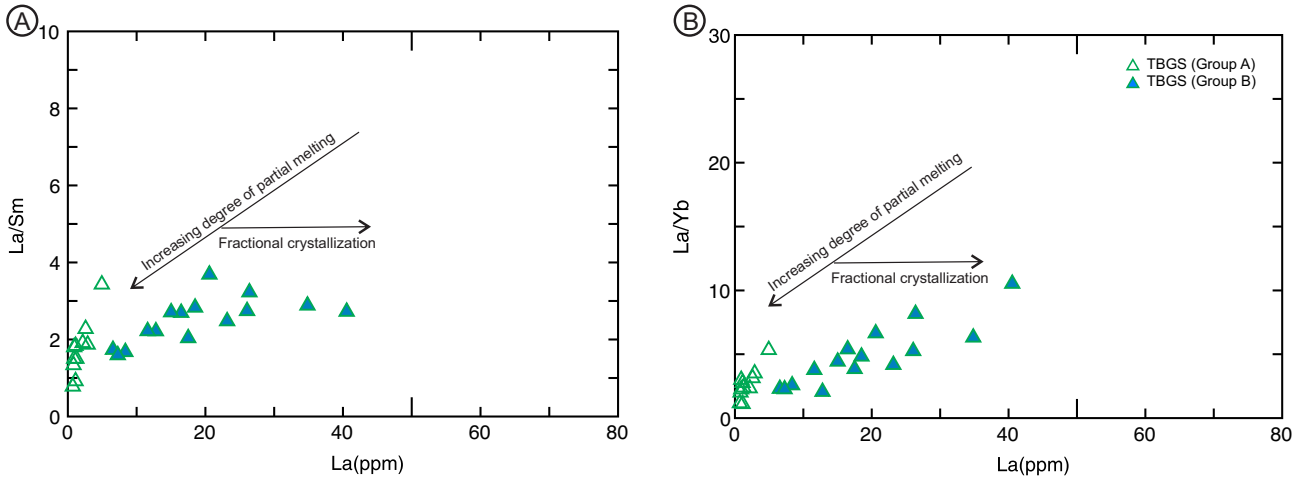

unaffected by fractional crystallization or partial melting. The TBGS samples have enriched mid-ocean ridge basalt (E-MORB) to ocean-island basalt (OIB) chemical affinities, including elevated $(La/Yb)_{cn}$ and negligible Nb, Ti, and Eu anomalies on extended trace element and REE diagrams (Fig. 10). The samples typically plot near E-MORB on trace element discrimination diagrams (Figs. 13A and 13B). They exhibit low $(Tb/Yb)_{cn}$ ratios (Fig. 13C), which indicate relatively small melt fractions and/or the absence of garnet in the source melt, suggesting that the melting occurred in the spinel stability field, at depths typically less than 80 km (Zhang et al. 2008). Moreover, the TBGS samples display moderate $(La/Sm)_{pm}$ (largely > 1), which, when interpreted together with the REE patterns, supports their derivation of the primary melts of the TBGS from modest degrees of partial melting of an enriched mantle source (Fig. 13D).

The isotopic signatures for the TBGS are mostly juvenile with $\varepsilon Nd_{(430\ Ma)}$ ranging from −1.1 to +6.4 and $^{87}Sr/^{86}Sr_{(i)}$ values ranging from 0.703373 to 0.708250, with one sample having an $\varepsilon Nd_{(430\ Ma)}$ of −8.6 (Fig. 11). Their isotopic variability may either reflect variability in the mantle source or, alternatively, a role for minor lithospheric contamination. Their collective geochemical compositions are consistent with their primary derivation from an enriched mantle source.

E-MORB compositions are believed to originate from a depleted asthenospheric mantle that has been refertilized by enriched components related to subduction, or they may also represent a lower degree of partial melting of a normal mid-ocean ridge basalt (N-MORB) mantle source (Saccani et al. 2013). The (Th/Ta)/(Th/Tb) ratios for the TBGS are <1 and are typical of N-MORB-derived rocks (Allègre and Minster 1978). This could suggest that the TBGS formed from a N-MORB-like source. However, N-MORB compositions typically have low $(La/Yb)_{pm}$ and $(Sm/Yb)_{pm}$ ratios whereas those for the TBGS are much higher, negating the possibility of partial melting of an N-MORB mantle source. The TBGS samples show LREE/HREE enrichment and have greater LREE enrichment than that of N-MORB (Fig. 10D), indicative of an E-MORB mantle source.

Fig. 13. (A) Zr/Y versus Nb/Y diagram (Fitton et al. 1997). (B) Th/Yb versus Zr/Yb Pearce 2008. (C) La_{cn}/Sm_{cn} versus Tb_{cn}/Yb_{cn} (Zhang et al. 2008). (D) TiO_2/Yb versus Th/Nb diagram (Pearce 2021). The black squares represent average end-member compositions given by Pearce et al. (2021). The black double-headed arrow represents a mixing line between IAB and OIB + OPB end-member sources. IAB, Island Arc Basalts; OPB, ocean plateau basalts; and SZLM, subduction-modified lithospheric mantle. S, subduction component; C, crustal contaminant component; W, within plate; f, fractional crystallization; UCC, upper continental crust; BCC, bulk continental crust; LCC, lower continental crust. Continental crust values from Taylor and McLennan (1995).

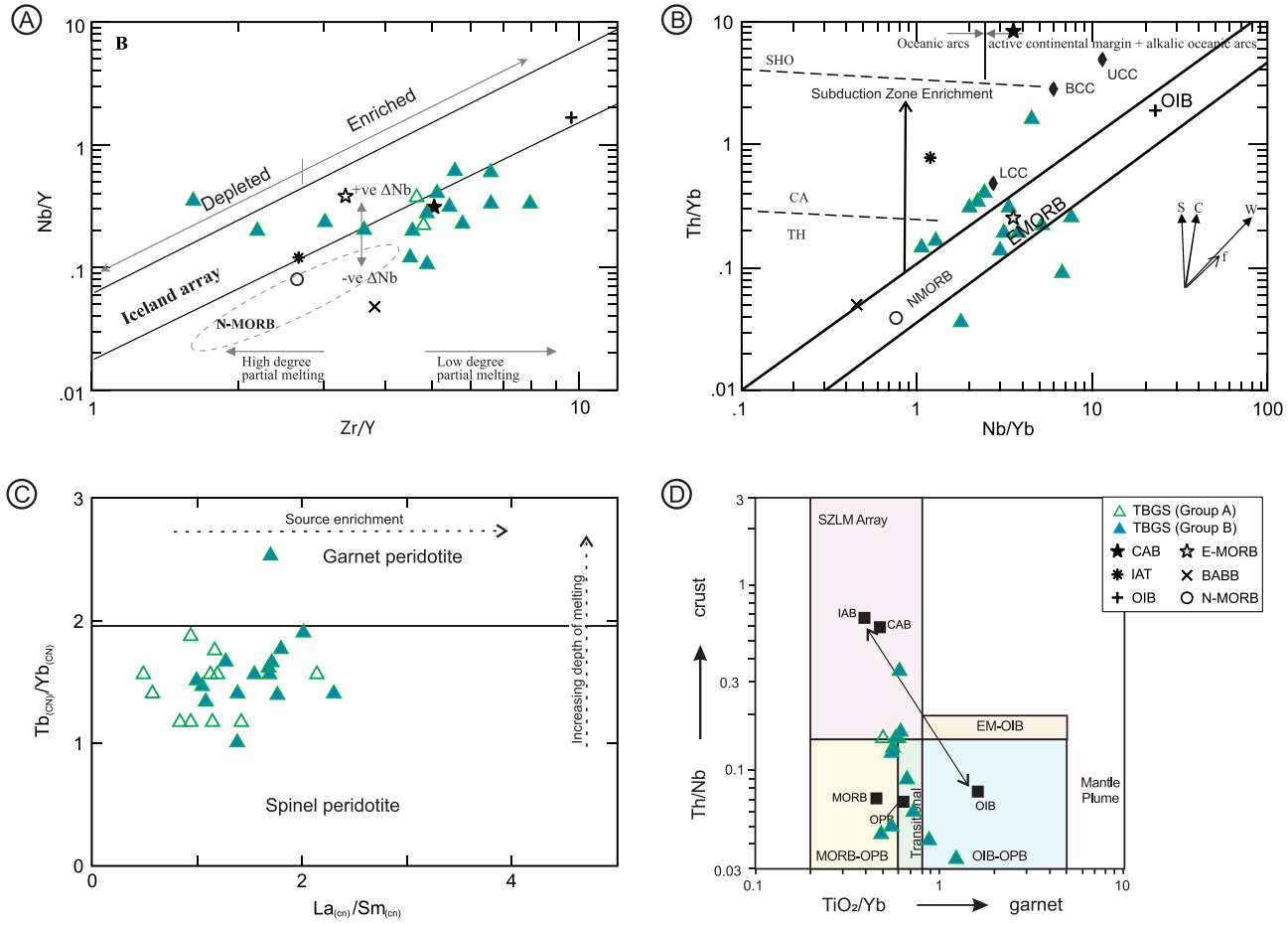

The predominantly positive $\varepsilon Nd_{(430\ Ma)}$ values observed in the samples are generally consistent with a relatively depleted mantle source; however, on trace element ratio diagrams they plot towards a more enriched mantle source (Figs. 13A and 13B). Mantle plume enrichment is typically associated with an OIB chemical signature. This suggests the source for the TBGS is a depleted asthenospheric mantle that has been refertilized by subduction zone enrichment. This dual influence produces a mixed geochemical signature, combining characteristics of both depleted (e.g., high εNd) and enriched mantle components (e.g., elevated incompatible element ratios; Fig. 13D).

6.2. Petrogenesis of the silicic rocks

The silicic samples are all granitic and display negative Nb, Ti, and Eu anomalies, signatures typically associated with crustal-derived melts. They are magnesian, metaluminous, and alkali calcic in composition (Fig. 9C). Depletion of Nb and Ti are interpreted as arc-type signatures in silicic rocks but can also arise from the anatexis of rocks with arc parentage (Whalen et al. 1998; Morris and Ryan 2003) or through lithospheric contamination of a mantle-derived melt. In silicic magmas, an abundance of large ion lithophile elements and elevated LREEs are typically attributed to the input of fluids or melts derived from crustal sources, related either to subduction processes or to intra-crustal contamination (Zamboni et al. 2016). On multi-element and REE plots, the silicic rocks have patterns typical of melts derived by partial melting of a sialic crust (Figs. 9E and 9F; Menuge et al. 2002; Brewer et al. 2004). The $\varepsilon Nd_{(t\ =\ 430\ Ma)}$ values for the silicic rocks plot between depleted mantle and Grenvillian basement (Fig. 11), suggesting minor involvement of Grenville crust in their genesis. The silicic samples have elevated Y and $Yb_{(CN)}$ but low Sr/Y and $(La/Yb)_{CN}$ (supplemental material S6), a classic signature of fractional crystallization of an intermediate melt (e.g., tonalitic) under shallow crustal conditions where plagioclase and amphibole dominate the mineral assemblage, but garnet is absent (Drummond and Defant 1990; Drummond et al. 1996). This suggests that the silicic samples are derived in part via partial melting and/or assimilation of minor amounts of Grenvillian basement rocks of the Long Range Inlier.

The silicic magmatism has been proposed to be correlative with the Sops Arm Group silicic volcanic rocks (Heaman et al. 2002). The new geochronology data presented herein suggest that the granitic magmatism is ~10 m.y. younger than the Sops Arm Group. The ca. 419 Ma age of magmatism is the youngest Silurian magmatism known in the area. Magmatism of this age is documented throughout Ganderian margin (see Wang et al. 2024). Whether the quartz–feldspar porphyry rhyolites are synchronous with the Sops Arm Group or the younger ca. 419 Ma magmatism remains unknown.

6.3. Timing of Silurian magmatism

The TBGS intruded the Laurentian margin into the Mesoproterozoic to Neoproterozoic (Tonian) basement of the Long Range Inlier. The geochronological data presented herein indicate that although TBGS is multiphase and the intrusive dynamics and history is complex, the timing of intrusion is well constrained to 431.0 ± 2.7/4.3 Ma, overlapping with previously reported bulk zircon physical abrasion TIMS zircon age from a fine-grained phase along the margin of the intrusion at 430.5 ± 2.5 Ma (Heaman et al. 2002). Therefore, despite the heterogeneous, multiphase intrusive history of the TBGS, it appears to represent a short-lived magmatic event. The cross-cutting silicic magmatism is constrained to 419.7 ± 2.7/4.3 Ma. The extent of this silicic magmatic event in the Long Range Inlier is unknown. Still, it may be related to other poorly temporally constrained intrusive units in the region (e.g., Gull Lake Intrusive Suite or Devils Room granite).

This ca. 430 Ma (Homerian) magmatic event has been documented east of the TBGS in both the peri-Laurentian and peri-Gondwanan segments of the Dunnage Zone (Dunning et al. 1990; Lissenberg et al. 2006; Sandeman et al. 2024; Wang et al. 2024). This confirms that a Homerian asthenospheric upwelling, likely driven by slab rollback, is recognized in western and central Newfoundland (Whalen et al. 2006; van Staal et al. 2014; Sandeman et al. 2024). This Homerian magmatic event is also documented along the entire northern Appalachian orogen (Rankin et al. 2007; Karabinos et al. 2008; Castonguay et al. 2014; Dorais et al. 2017; Wilson et al. 2017).

6.4. Geodynamic implications

In western Newfoundland, the LR-CF system is interpreted to record major net dextral strike-slip movement of the Dashwoods terrane\Notre Dame arc along the Laurentian margin during Ordovician to Carboniferous (Brem et al. 2007; Lin et al. 2013; van Staal and Zagorevski 2020). Restoration of movement along these faults amounts to between 200 and 300 km of slip (Waldron et al. 2015), indicating that during the Silurian, the Long Range Inlier was proximal to the southern Dashwoods or perhaps farther southwest (present-day orientation). The nature of the LR-CF system as a crustal-scale discontinuity that extends into the upper mantle is evidenced by seismic reflection data supporting the interpretation that the LR-CF system is a deep transcurrent fault, which formed during oblique convergence and terrane accretion during Taconic to Acadian orogenesis (Stockmal et al. 1990; Waldron and Stockmal 1994; Barr et al. 2014). Inherited deep crustal structures repeatedly serve as zones of deformation and reactivation during orogenesis (Thomas 2006; Hatcher 2010; Guillaume et al. 2022).

In regions characterized by inherited deep crustal structures, such as the DVF/LR-CF systems, mafic magmatism can be driven by a combination of transtensional tectonics, lithospheric extension and rifting, and reactivation of pre-existing structural fabrics (Matton and Jébrak 2009). Continental-scale strike-slip faults and shear zones in orogenic belts typically develop as a result of the continuing movement of foundational lithospheric blocks (terranes) within the developing orogen. The strike-slip faults in western Newfoundland, such as LR-CF system, for the most part follow the boundary zone between lithosphere of differing thickness, age, and internal structure and represent major crustal and lithospheric discontinuities that likely constitute corridors/conduits along which mantle melts can ascend or flow laterally (Murphy 2003; Rocchi et al. 2003; Pirajno 2010). These melts would eventually be focused at the mantle–crust and lithosphere–asthenosphere boundaries. Although a seismic lithoprobe line across the LR-CF system in the southern Humber Zone indicates a boundary zone of differing lithospheric thickness (van der Velden et al. 2004; Brem 2007), whether this difference is reflected across the DVF system is unknown.

During the late Silurian, and immediately after the terminal Iapetan closure, amalgamated Laurentian, peri-Laurentian, and peri-Gondwanan terranes (excluding Avalonia) of the Newfoundland Appalachians record voluminous, largely bi-modal, eastward-younging and extension-related, non-arc-like magmatism attributed to slab rollback or breakoff (Lissenberg et al. 2006; Whalen et al. 2006; van Staal et al. 2014; Honsberger et al. 2022; Sandeman et al. 2024). The formation of the TBGS is inferred to be contemporaneous with this magmatic event, indicative of extension in the upper plate (Laurentian margin). Extension in the eastern Humber/Laurentian margin would likely have utilized pre-existing structures. Slab rollback would create a window beneath the extending upper plate, allowing local asthenospheric upwelling, which introduced heat and partial melting of the subcontinental lithospheric mantle. The precursor to the DVF system would have enabled locally focused, decompressional partial melting and subsequently acted as a pathway(s) for the ascent of derivative mafic magmas of the TBGS. The TBGS laccolith formation may have been focused in the area because of ponding of the magma batches near the structural brittle–ductile transition zone along a northwest-trending fault zone conjugate to the DVF and LR-CF systems. This is the only known occurrence of magmatism of this age in the Long Range Inlier of western Newfoundland.

7. Conclusions

Field, petrographic, U–Pb geochronological data, mineral chemistry, and lithogeochemical and isotopic data for the TBGS provide new insights into Silurian magmatism in the Laurentian margin of western Newfoundland. The TBGS is a multiphase, heterogeneous, cumulate, northwest-trending oblong body that intrudes the Proterozoic Long Range Inlier. The complex, co-mingling relationships along with the U–Pb zircon SHRIMP ages indicate that although the intrusion con-

tains multiple phases, the gabbroic components of the suite represent a single brief magmatic event at ca. 431.0 ± 2.9/4.3 Ma that was subsequently intruded by slightly younger, minor silicic magmatism at 419.7 ± 3.0/4.5 Ma. Mineral chemical and lithogeochemical data indicate that the predominant control on compositional evolution of the rocks of the TBGS was fractional crystallization of olivine + clinopyroxene + feldspar and Fe–Ti oxides. The suite is tholeiitic and transitional to calc-alkaline, non-arc-like, continental magmas derived from an E-MORB-like source. This is supported by the largely positive $\varepsilon Nd_{(430\ cMa)}$ ratios and primitive Sr isotopic compositions. The silicic samples are granitic, magnesian, and alkali calcic in composition, likely reflecting partial melting and/or assimilation of feldspathic, meta-igneous middle to upper crustal Proterozoic basement rocks. The ~10-million-year age gap between mafic and silicic magmatism indicates that the silicic magmatism is not likely a direct result of mafic magmatism melting the crust, although this cannot be ruled out.

Following the terminal closure of the Iapetus Ocean and associated seaways, the TBGS formed as a result of extensional tectonics along the Laurentian margin. Slab rollback would have created a window beneath the extending upper plate, promoting local asthenospheric upwelling, which introduced heat and partial melting of the subcontinental lithospheric mantle. The precursor to the DVF system, a zone of inherited structural weakness, would have facilitated localized adiabatic decompressional melting within the upper asthenosphere and subsequently acted as a pathway(s) for the ascent and emplacement of mantle-derived mafic magmas.

Acknowledgements

This research was funded by the Geological Survey of Newfoundland and Labrador (GSNL). Kim Morgan and Evie Li are thanked for their cartographic support. Internal reviews by colleagues at the Geological Survey (Gabriel Santos and Chris Pereira) and Geological Survey of Canada (Bill Davis) greatly improved the clarity of the manuscript. External reviews by Cees van Staal and two anonymous reviewers further improved the manuscript. Comments and handling of the manuscripts by Editor Sally Perhsson were equally appreciated.

Article information

History dates

Received: 6 March 2025
Accepted: 12 October 2025
Accepted manuscript online: 24 October 2025
Version of record online: 23 December 2025

Copyright

Data availability

Data are available from the GSNL Geological Atlas located at: https://geoatlas.gov.nl.ca.

Author information

Author ORCIDs

A.M. Hinchey https://orcid.org/0000-0003-3826-0724
H.A. Sandeman https://orcid.org/0000-0002-2375-2243

Author notes

A.M. Hinchey served as Associate Editor at the time of manuscript review and acceptance; peer review and editorial decisions regarding this manuscript were handled by another editorial board member.

Author contributions

Conceptualization: AMH, CJL
Data curation: AMH
Formal analysis: AMH, NR, DMM
Investigation: AMH, JGH
Methodology: AMH, NR, DMM
Validation: AMH, JGH, HAS, CJL
Visualization: AMH, JGH, HAS, CJL
Writing – original draft: AMH
Writing – review & editing: AMH, JGH, HAS, CJL, NR, DMM

Competing interests

There are no competing interests.

Supplementary material

Supplementary data are available with the article at https://doi.org/10.1139/cjes-2025-0016.

References

Allègre, C.J., and Minster, J.F. 1978. Quantitative models of trace element behavior in magmatic processes. Earth and Planetary Science Letters, **38**: 1–25. doi:10.1016/0012-821X(78)90123-1.

Barr, S.M., Dehler, S.A., and Zsámboki, L. 2014. Connecting Cape Breton Island and Newfoundland, Canada: geophysical modeling of pre-Carboniferous "basement" rocks in the Cabot Strait Area. Geoscience Canada, **41**: 186. doi:10.12789/geocanj.2014.41.041.

Black, L.P., Kamo, S.L., Williams, I.S., Mundil, R., Davis, D.W., Korsch, R.J., and Foudoulis, C. 2003. The application of SHRIMP to Phanerozoic geochronology; a critical appraisal of four zircon standards. Chemical Geology, **200**: 171–188. doi:10.1016/S0009-2541(03)00166-9.

Brem, A. 2007. The Late Proterozoic to Palaeozoic Tectonic Evolution of the Long Range Mountains in Southwestern Newfoundland. University of Waterloo.

Brewer, T.S., Åhäll, K.I., Menuge, J.F., Storey, C.D., and Parrish, R.R. 2004. Mesoproterozoic bimodal volcanism in SW Norway, evidence for recurring pre-Sveconorwegian continental margin tectonism. Precambrian Research, **134**: 249–273. doi:10.1016/j.precamres.2004.06.003.

Castonguay, S., Van Staal, C.R., Joyce, N., Skulski, T., and Hibbard, J.P. 2014. Taconic metamorphism preserved in the Baie Verte Peninsula, Newfoundland Appalachians: geochronological evidence for ophiolite obduction and subduction and exhumation of the leading edge of the Laurentian (Humber) margin during closure of the Taconic seaway. Geoscience Canada, **41**: 459–482. doi:10.12789/geocanj.2014.41.055.

Cicconi, M.R., Losq, C.L., Henderson, G.S., and Neuville, D.R. 2021. Magma redox geochemistry. *In* Magma redox geochemistry. Wiley. pp. 381–398. doi:10.1002/9781119473206.ch19.

Collins, P.G. 2007. A petrographic and geochemical characterization and the evaluation of the exploralion potential for nickel sulfides in several mafic-ultramafic intrusive complexes in Newfoundland. Cambridge.

Colman-Sadd, S.P., Hayes, J.P., and Knight, I. 1990. Geology of the Island of Newfoundland. Government of Newfoundland and Labrador, Department of Mines and Energy, Geological Survey Branch, Map 90-001.

DePaolo, D.J. 1988. Neodymium isotope geochemistry. Minerals, rocks and mountains. Springer, Berlin, Heidelberg.

Dickin, A.P. 2004. Mesoproterozoic and Paleoproterozoic crustal growth in the eastern Grenville Province: Nd isotope evidence from the Long Range inlier of the Appalachian orogen. *In* Memoir of the Geological Society of America. Vol. 197. pp. 495–503. doi:10.1130/0-8137-1197-5.495.

Dorais, M.J., Marvinney, R.G., and Markert, K. 2017. The age, petrogeneis and tectonic significance of the Frontenac Formation basalts, northern New Hampshire and western Maine. American Journal of Science, **317**: 990–1018. doi:10.2475/09.2017.02.

Drummond, M.S., and Defant, M.J. 1990. A model for Trondhjemite-Tonalite-Dacite Genesis and crustal growth via slab melting: Archean to modern comparisons. Journal of Geophysical Research: Solid Earth, **95**: 21503–21521. doi:10.1029/JB095iB13p21503.

Drummond, M.S., Defant, M.J., and Kepezhinskas, P.K. 1996. Petrogenesis of slab-derived trondhjemite–tonalite–dacite/adakite magmas. Earth and Environmental Science Transactions of The Royal Society of Edinburgh, **87**: 205–215. doi:10.1017/s0263593300006611.

Dunning, G.R. 1987. U/Pb geochronology of the Coney Head Complex, Newfoundland. Canadian Journal of Earth Sciences, **24**: 1072–1075. doi:10.1139/e87-104.

Dunning, G.R., O'Brien, S.J., Colman-Sadd, S.P., Blackwood, R.F., Dickson, W.L., O'Neill, P.P., and Krogh, T.E. 1990. Silurian orogeny in the Newfoundland Appalachians. The Journal of Geology, **98**: 895–913. doi:10.1086/629460.

Erdmer, P. 1986. Geology of the Long Range Inlier in Sandy Lake map area, western Newfoundland. G.S.O., Canada.

Erdmer, P., and Williams, H. 1995. Grenville basement rocks (Humber Zone). *In* Geology of the Appalachian–Caledonian Orogen in Canada and Greenland. Geological Survey of Canada. pp. 51–63.

Ewart, A., Collerson, K.D., Regelous, M., Wendt, J.I., and Niu, Y. 1998. Geochemical Evolution within the Tonga-Kermadec-Lau Arc-Back-arc Systems: the role of varying mantle wedge composition in space and time. Journal of Petrology, **39**: 331–368. doi:10.1093/petroj/39.3.331.

Fitton, J.G., Saunders, A.D., Norry, M.J., Hardarson, B.S., and Taylor, R.N. 1997. Thermal and chemical structure of the Iceland plume. Earth and Planetary Science Letters, **153**: 197–208. doi:10.1016/S0012-821X(97)00170-2.

Frost, B.R., and Frost, C.D. 2008. A geochemical classification for feldspathic igneous rocks. Journal of Petrology, **49**: 1955–1969. doi:10.1093/petrology/egn054.

Goldstein, S.L., O'Nions, R.K., and Hamilton, P.J. 1984. A Sm–Nd isotopic study of atmospheric dusts and particulates from major river systems. Earth and Planetary Science Letters, **70**: 221–236. doi:10.1016/0012-821X(84)90007-4.

Guillaume, B., Gianni, G.M., Kermarrec, J.-J., and Bock, K. 2022. Control of crustal strength, tectonic inheritance, and stretching/shortening rates on crustal deformation and basin reactivation: insights from laboratory models. Solid Earth, **13**: 1393–1414. doi:10.5194/se-13-1393-2022.

Hatcher, R.D. 2010. The Appalachian orogen: a brief summary. *In* Memoir of the Geological Society of America. Vol. 206. pp. 1–19. doi:10.1130/2010.1206(01).

Heaman, L.M., and LeCheminant, A.N. 1993. Paragenesis and U–Pb systematics of baddeleyite (ZrO2). Chemical Geology, **110**: 95–126. doi:10.1016/0009-2541(93)90249-I.

Heaman, L.M., Bowins, R., and Crocket, J. 1990. The chemical composition of igneous zircon suites: implications for geochemical tracer studies. Geochimica et Cosmochimica Acta, **54**: 1597–1607. doi:10.1016/0016-7037(90)90394-Z.

Heaman, L.M., Erdmer, P., and Owen, J.V. 2002. U–Pb geochronologic constraints on the crustal evolution of the Long Range Inlier, Newfoundland. Canadian Journal of Earth Sciences, **39**: 845–865. doi:10.1139/e02-015.

Hinchey, A.M. 2010. Geology of the Northern Portion of the Silver Mountain Map area (NTS 12H/11), Southern Long Range Inlier, Newfoundland. Current Research (2010) Newfoundland and Labrador Department of Natural Resources Geological Survey, Report 10-1. pp. 245–263. doi:10.13140/RG.2.2.18689.07520.

Hinchey, A.M. 2020. Geology of the Northern Silver Mountain Map Area (NTS 12H/11). Scale 1:50 000. Newfoundland and Labrador, Department of Industry, Energy and Technology, Geological Survey, Map 2020-18, Open File, 12H/11:1. doi:10.13140/RG.2.2.18689.07520.

Hinchey, A.M., Knight, I., Sandeman, H.A., and Hinchey, J.G. 2022. Tournaisian volcanism associated with transtensional basin development in western Newfoundland during the amalgamation of Pangea. Gondwana Research, **110**: 226–248. doi:10.1016/j.gr.2022.06.013.

Hinchey, A.M., Serna Ortiz, S., Skipton, D., and Mendoza Marin, D. 2025. Metasedimentary sequences in the Long Range Inlier: Detrital zircon evidence for post-Grenvillian sedimentary deposition. Current Research (2025), Newfoundland and Labrador Department of Industry, Energy and Technology, Geological Survey, Report, 25-1. pp. 115–130. doi:10.13140/RG.2.2.25937.03683.

Holder, R.M., Yakymchuk, C., and Viete, D.R. 2020. Accessory mineral Eu anomalies in suprasolidus rocks: beyond feldspar. Geochemistry, Geophysics, Geosystems, **21**. doi:10.1029/2020gc009052.

Honsberger, I.W., Bleeker, W., Kamo, S.L., Sandeman, H.A.I., Evans, D.T.W., Rogers, N., et al. 2022. Latest Silurian syntectonic sedimentation and magmatism and Early Devonian orogenic gold mineralization, central Newfoundland Appalachians, Canada: setting, structure, lithogeochemistry, and high-precision U–Pb geochronology. GSA Bulletin, **134**: 2933–2957. doi:10.1130/b36083.1.

Hyde, R.S., Miller, H.G., Hiscott, R.N., and Wright, J.A. 2007. Basin architecture and thermal maturation in the strike-slip Deer Lake Basin, Carboniferous of Newfoundland. Basin Research, **1**: 85–105. doi:10.1111/j.1365-2117.1988.tb00007.x.

Jensen, L.S. 1976. A new cation plot for classifying subalkalic volcanic rocks. Ontario Division Mines, Miscellaneous Paper. Vol. 66. p. 22.

Kamo, S.L., Gower, C.F., Kamo, S.L., and Gower, C.F. 1994. Note: U–Pb baddeleyite dating clarifies age of characteristic paleomagnetic remanence of Long Range dykes, southeastern Labrador. Atlantic Geology, **30**: 259–262. doi:10.4138/2133.

Karabinos, P., Morris, D., Hamilton, M., and Rayner, N. 2008. Age, origin, and tectonic significance of Mesoproterozoic and Silurian felsic sills in the Berkshire massif, Massachusetts. American Journal of Science, **308**: 787–812. doi:10.2475/06.2008.03.

Lin, S., Brem, A.G., van Staal, C.R., Davis, D.W., McNicoll, V.J., and Pehrsson, S. 2013. The Corner Brook Lake block in the Newfoundland Appalachians: A suspect terrane along the Laurentian margin and evidence for large-scale orogen-parallel motion Geological Society of America Bulletin, **125**(9-10): 1618–1632. doi:10.1130/B30805.1.

Lissenberg, C.J., McNicoll, V.J., and van Staal, C.R. 2006. The origin of mafic–ultramafic bodies within the northern Dashwoods subzone, Newfoundland Appalachians. Atlantic Geology, **42**: 1–12. doi:10.4138/2152.

Ludwig, K. 2012. User's manual for Isoplot/Ex rev. 3.70: a geochronological toolkit for Microsoft Excel. *In* Special Publication 5. Berkeley Geochronology Center, Berkeley. pp. 1–76.

Matton, G., and Jébrak, M. 2009. The Cretaceous Peri-Atlantic Alkaline Pulse (PAAP): deep mantle plume origin or shallow lithospheric break-up? Tectonophysics, **469**: 1–12. doi:10.1016/j.tecto.2009.01.001.

Menuge, J.F., Brewer, T.S., and Seeger, C.M. 2002. Petrogenesis of metaluminous A-type rhyolites from the St Francois Mountains, Missouri and the Mesoproterozoic evolution of the southern Laurentian margin. Precambrian Research, **113**: 269–291. doi:10.1016/s0301-9268(01)00211-x.

Middlemost, E.A.K. 1994. Naming materials in the magma/igneous rock system. Earth-Science Reviews, **37**: 215–224. doi:10.1016/0012-8252(94)90029-9.

Morimoto, N. 1988. Nomenclature of pyroxenes. Mineralogy and Petrology, **39**: 55–76. doi:10.1007/BF01226262.

Morris, J.D., and Ryan, J.G. 2003. Subduction zone processes and implications for changing composition of the upper and lower mantle. *In* Treatise on geochemistry. Elsevier. pp. 451–470.

Moyen, J.-F., Janoušek, V., Laurent, O., Bachmann, O., Jacob, J.-B., Farina, F., et al. 2021. Crustal melting vs. fractionation of basaltic magmas: Part 1, granites and paradigms. Lithos, **402–403**: 106291. doi:10.1016/j.lithos.2021.106291.

Müntener, O., Kelemen, P.B., and Grove, T.L. 2001. The role of H2O during crystallization of primitive arc magmas under uppermost mantle conditions and genesis of igneous pyroxenites: an experimental study. Contributions to Mineralogy and Petrology, **141**: 643–658. doi:10.1007/s004100100266.

Murphy, J.B. 2003. Late Palaeozoic formation and development of the St Marys Basin, mainland Nova Scotia, Canada: a prolonged record of intracontinental strike-slip deformation during the assembly of Pangaea, Vol. **210**, Special Publications, Geological Society, London, pp. 185–196. doi:10.1144/gsl.Sp.2003.210.01.11.

Murphy, J.B., Keppie, J.D., Nance, R.D., and Dostal, J. 2010. Comparative evolution of the Iapetus and Rheic Oceans: a North America perspective. Gondwana Research, **17**: 482–499. doi:10.1016/j.gr.2009.08.009.

Murphy, J.B., van Staal, C.R., and Duncan Keppie, J. 1999. Middle to late Paleozoic Acadian orogeny in the northern Appalachians: a Laramide-style plume-modified orogeny? Geology, **27**: 653–656. doi:10.1130/0091-7613(1999)027⟨0653:Mtlpao⟩2.3.Co;2.

Owen, J.V. 1991. Geology of the Long Range Inlier, Newfoundland. *In* Geological Survey of Canada, Bulletin 395. p. 89.

Pearce, J.A. 2008. Geochemical fingerprinting of oceanic basalts with applications to ophiolite classification and the search for Archean oceanic crust. Lithos, **100**(1–4): 14–48. doi:10.1016/j.lithos.2007.06.016.

Pearce, J.A., Ernst, R.E., Peate, D.W., and Rogers, C. 2021. LIP printing: Use of immobile element proxies to characterize Large Igneous Provinces in the geologic record. Lithos, **393**: 106068. doi:10.1016/j.lithos.2021.106068.

Pirajno, F. 2010. Intracontinental strike-slip faults, associated magmatism, mineral systems and mantle dynamics: examples from NW China and Altay-Sayan (Siberia). Journal of Geodynamics, **50**: 325–346. doi:10.1016/j.jog.2010.01.018.

Rankin, D.W., Coish, R.A., Tucker, R.D., Peng, Z.X., Wilson, S.A., and Rouff, A.A. 2007. Silurian extension in the Upper Connecticut Valley, United States and the origin of middle Paleozoic basins in the Québec embayment. American Journal of Science, **307**: 216–264. doi:10.2475/01.2007.07.

Rocchi, S., Storti, F., Di Vincenzo, G., and Rossetti, F. 2003. Intraplate strike-slip tectonics as an alternative to mantle plume activity for the Cenozoic rift magmatism in the Ross Sea region, Antarctica. Vol. 210. Geological Society, London, Special Publications. pp. 145–158. doi:10.1144/gsl.Sp.2003.210.01.09.

Rudnick, R.L., and Gao, S. 2003. Composition of the continental crust. *In* Treatise on Geochemistry. Vol. 3–9. pp. 1–64. doi:10.1016/B0-08-043751-6/03016-4.

Saccani, E., Azimzadeh, Z., Dilek, Y., and Jahangiri, A. 2013. Geochronology and petrology of the Early Carboniferous Misho Mafic Complex (NW Iran), and implications for the melt evolution of Paleo-Tethyan rifting in Western Cimmeria. Lithos, **162–163**: 264–278. doi:10.1016/j.lithos.2013.01.008.

Sandeman, H.A.I., and Dunning, G.R. 2016. Preliminary U–Pb geochronology and petrochemistry of volcanic rocks and felsic dykes of the Silurian Sops Arm Group, White Bay, western Newfoundland (NTS 2H/10 and 15). Current Research, Newfoundland and Labrador Department of Natural Resources Geological Survey, Report 16-1. pp. 39–69. doi:10.13140/RG.2.1.2380.2642.

Sandeman, H.A.I., Honsberger, I.W., Peddle, C., Kamo, S.L., and Dunning, G.R. 2024. Petrochemical and geochronological constraints on the origin of the Sops Arm group, the most westerly Silurian volcanosedimentary extensional basin on the western Newfoundland composite Laurentian margin. Canadian Journal of Earth Sciences. doi:10.1139/cjes-2024-0032.

Smyth, W.R., and Schillereff, H.S. 1982. The Pre-Carboniferous geology of southwest White Bay. Current Research, Government of Newfoundland and Labrador, Department of Mines and Energy, Mineral Development Division, Report 82-01.

Stockmal, G.S., Colman-Sadd, S.P., Keen, C.E., Marillier, F., O'Brien, S.J., and Quinlan, G.M. 1990. Deep seismic structure and plate tectonic evolution of the Canadian Appalachians. Tectonics, **9**: 45–62. doi:10.1029/TC009i001p00045.

Stolz, A.J., Varne, R., Davies, G.R., Wheller, G.E., and Foden, J.D. 1990. Magma source components in an arc-continent collision zone: the Flores-Lembata sector, Sunda arc, Indonesia. Contributions to Mineralogy and Petrology, **105**: 585–601. doi:10.1007/BF00302497.

Sun, S.-S., and McDonough, W.F. 1989. Chemical and isotopic systematics of oceanic basalts: implications for mantle composition and processes. Geological Society, London, Special Publications. Vol. 42. pp. 313–345. doi:10.1144/GSL.SP.1989.042.01.19.

Taylor, S.R., and McLennan, S.M. 1995. The geochemical evolution of the continental crust. Reviews of Geophysics, **33**: 241. doi:10.1029/95RG00262.

Terakado, Y., and Fujitani, T. 1995. Significance of iron and cobalt partitioning between plagioclase and biotite for problems concerning the Eu2+/Eu3+ ratio, europium anomaly, and magnetite-/ilmenite-series designation for granitic rocks from the Inner Zone of southwestern Japan. Geochimica et Cosmochimica Acta, **59**: 2689–2699. doi:10.1016/0016-7037(95)00165-V.

Thomas, W.A. 2006. Tectonic inheritance at a continental margin. GSA Today, **16**: 4. doi:10.1130/1052-5173(2006)016[4:Tiaacm]2.0.Co;2.

van der Velden, A.J., van Staal, C.R., and Cook, F.A. 2004. Crustal structure, fossil subduction, and the tectonic evolution of the Newfoundland Appalachians: evidence from a reprocessed seismic reflection survey. Geological Society of America Bulletin, **116**: 1485–1498. doi:10.1130/B25518.1.

van Staal, C.R., and Barr, S.M. 2012. Lithospheric architecture and tectonic evolution of the Canadian Appalachians and associated Atlantic margin. *In* Tectonic styles in Canada: the LITHOPROBE perspective. *Edited by* J.A. Percival, F.A. Cook and R.M. Clowes. Geological Association of Canada, Special Paper 49. pp. 41–95.

van Staal, C.R., and Zagorevski, A. 2022. Paleozoic tectonic evolution of the rifted margins of Laurentia. *In* Laurentia: turning points in the evolution of a continent. Geological Society of America.

van Staal, C.R., Barr, S.M., Waldron, J.W.F., Schofield, D.I., Zagorevski, A., and White, C.E. 2021. Provenance and Paleozoic tectonic evolution of Ganderia and its relationships with Avalonia and Megumia in the Appalachian–Caledonide orogen. Gondwana Research, **98**: 212–243. doi:10.1016/j.gr.2021.05.025.

van Staal, C.R., Lin, S., Valverde-Vaquero, P., Dunning, G., Burgess, J., Schofield, D., and Joyce, N. 2024. Tectonic evolution of high-grade metamorphic tectonites of the Meelpaeg structure near Port aux Basques, southwestern Newfoundland during the Silurian Salinic and Early-to-Middle Devonian Acadian orogenies. Canadian Journal of Earth Sciences. doi:10.1139/cjes-2023-0141.

van Staal, C.R., Zagorevski, A., McNicoll, V.J., and Rogers, N. 2014. Time-transgressive Salinic and Acadian Orogenesis, magmatism and Old Red Sandstone sedimentation in Newfoundland. Geoscience Canada, **41**: 138–164. doi:10.12789/geocanj.2014.41.031.

Waldron, J.W.F., and Stockmal, G.S. 1994. Structural and tectonic evolution of the Humber Zone, western Newfoundland 2. A regional model for Acadian thrust tectonics. Tectonics, **13**: 1498–1513. doi:10.1029/94tc01505.

Waldron, J.W.F., Barr, S.M., Park, A.F., White, C.E., and Hibbard, J. 2015. Late Paleozoic strike-slip faults in Maritime Canada and their role in the reconfiguration of the northern Appalachian orogen. Tectonics, **34**: 1661–1684. doi:10.1002/2015tc003882.

Waldron, J.W.F., McCausland, P.J.A., Barr, S.M., Schofield, D.I., Reusch, D., and Wu, L. 2022. Terrane history of the Iapetus Ocean as preserved in the northern Appalachians and western Caledonides. Earth-Science Reviews, 104163, **233**. doi:10.1016/j.earscirev.2022.104163.

Wang, C., Wang, T., van Staal, C.R., Hou, Z., and Lin, S. 2024. Evolution of Silurian to Devonian magmatism associated with the Acadian orogenic cycle in eastern and southern Newfoundland Appalachians: Evidence for a three-stage evolution characterized by episodic hinterland- and foreland-directed migration of granitoid magmatism. Geological Society of America Bulletin, **136**: 4648–4670. doi:10.1130/b37336.1.

Whalen, J.B., McNicoll, V.J., van Staal, C.R., Lissenberg, C.J., Longstaffe, F.J., Jenner, G.A., and van Breeman, O. 2006. Spatial, temporal and geochemical characteristics of Silurian collision-zone magmatism, Newfoundland Appalachians: an example of a rapidly evolving mag-

matic system related to slab break-off. Lithos, **89**: 377–404. doi:10.1016/j.lithos.2005.12.011.

Whalen, J.B., Rogers, N., van Staal, C.R., Longstaffe, F.J., Jenner, G.A., and Winchester, J.A. 1998. Geochemical and isotopic (Nd, O) data from Ordovician felsic plutonic and volcanic rocks of the Miramichi Highlands: petrogenetic and metallogenic implications for the Bathurst Mining Camp. Canadian Journal of Earth Sciences, **35**: 237–252. doi:10.1139/e97-102.

White, L.T., and Ireland, T.R. 2012. High-uranium matrix effect in zircon and its implications for SHRIMP U–Pb age determinations. Chemical Geology, **306–307**: 78–91. doi:10.1016/j.chemgeo.2012.02.025.

Williams, H. 1995. Geology of the Appalachian–Caledonian Orogen in Canada and Greenland. Geological Society of America, London.

Wilson, R.A., van Staal, C.R., and Kamo, S.L. 2017. Rapid transition from the Salinic to Acadian orogenic cycles in the northern Appalachian Orogen: evidence from northern New Brunswick, American Journal of Science, **317**: 449–482. doi:10.2475/04.2017.02.

Zamboni, D., Gazel, E., Ryan, J.G., Cannatelli, C., Lucchi, F., Atlas, Z.D., et al. 2016. Contrasting sediment melt and fluid signatures for magma components in the Aeolian Arc: implications for numerical modeling of subduction systems. Geochemistry, Geophysics, Geosystems, **17**: 2034–2053. doi:10.1002/2016GC006301.

Zhang, X., Zhang, H., Tang, Y., Wilde, S.A., and Hu, Z. 2008. Geochemistry of Permian bimodal volcanic rocks from central Inner Mongolia, North China: implication for tectonic setting and Phanerozoic continental growth in Central Asian Orogenic Belt. Chemical Geology, **249**: 262–281. doi:10.1016/j.chemgeo.2008.01.005.